ELECTRICAL AND MAGNETIC PROPERTIES OF

Bi(Pb)SrCaCuO SUPERCONDUCTOR THIN FILM PRODUCED

BY SPUTTERING METHOD

by
GÜRCAN YILDIRIM

THESIS SUBMITTED TO
THE GRADUATE SCHOOL OF NATURAL AND APPLIED
SCIENCES
OF
THE ABANT İZZET BAYSAL UNIVERSITY
IN PARTIAL FULFILLMENT OF THE REQUIREMENTS FOR THE
DEGREE OF
DOCTOR OF PHILOSOPHY
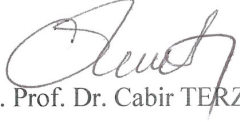IN
THE DEPARTMENT OF PHYSICS

OCTOBER 2012

Approval of the Graduate School of Natural and Applied Science

Prof. Dr. Yaşar DÜRÜST

Director

I certify that this thesis satisfies all the requirements as a thesis for the degree of Doctor of Philosophy.

Prof. Dr. Resul ERYİĞİT
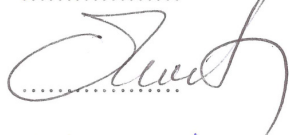
Head of Physics Department
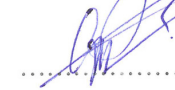
This is to certify that we have read this thesis and that in our opinion it is fully adequate, in scope and quality as a thesis for the degree of Doctor of Philosophy.

Assoc. Prof. Dr. Cabir TERZİOĞLU

Co-Supervisor

Prof. Dr. Ahmet VARİLCİ

Supervisor

Examining Committee Members:

1. Prof. Dr. Ahmet VARİLCİ

2. Assoc. Prof. Dr. Cabir TERZİOĞLU

3. Assoc. Prof. Dr. Yusuf ATALAY

4. Assist. Prof. Dr. Cihan PARLAK

5. Assist. Prof. Dr. Cevher ALTUĞ

ABSTRACT

ELECTRICAL AND MAGNETIC PROPERTIES OF

Bi(Pb)SrCaCuO SUPERCONDUCTOR THIN FILM PRODUCED

BY SPUTTERING METHOD

YILDIRIM, Gürcan

Doctor of Philosophy, Department of Physics

Supervisor: Prof. Dr. Ahmet VARİLCİ

Co-Supervisor: Assoc. Prof. Dr. Cabir TERZİOĞLU

The main objective of this thesis is to not only determine the optimum annealing ambient for the Bi(Pb)SrCaCuO superconductor thin film production but investigate the electrical, physical, microstructural, pinning mechanism and superconducting properties of the thin films produced by sputtering method at 100 watt DC power by means of scanning electron microscopy (SEM), X-Ray diffraction analysis (XRD), electron dispersive X-Ray (EDX), resistivity and transport critical current density measurements for applications in technology and industry, as well. In the first stage, after the literature research, we determined the various annealing time (15 min, 1.5 h and 3 h) and temperature (850, 860 and 870°C) to produce the Bi(Pb)SrCaCuO film obtaining the best surface morphology and superconducting properties. The measurements given above are carried out on the 9 films produced. Experimental results obtained show that the superconductor film annealed at 860°C

for 3 h exhibits the greatest Bi-2223 phase fraction, highest critical temperature, critical current density, best texturing, crystallinity and connectivity between grains, largest grain size and lowest porosity. In the second stage, the pinning mechanism and superconducting properties of the Bi-2223 thin film annealed at 860°C for 3 h are analyzed with the aid of the magnetoresistivity measurements conducted at several applied magnetic fields in a range of 0-3 T as a function of temperature changing from 20 to 130 K. The onset (T_c^{onset}) and offset (T_c^{offset}) critical temperatures, variation of the critical temperature, activation energy (U_0), irreversibility field ($\mu_0 H_{irr}$), upper critical field ($\mu_0 H_{c2}$), penetration depth (λ) and coherence length (ξ) of the film are evaluated from the magnetoresistivity curves. It is found that the superconducting properties degrade with the increment in the applied magnetic field as a result of the weak links between the superconducting grains in the sample. In the last stage, atomic force microscopy (AFM), magnetoresistivity and transport critical current density measurements as a function of the magnetic field direction (dc magnetic field and the angle between the surface of the film and the applied magnetic field) are performed to examine the anisotropic nature of the Bi-2223 film produced. The field direction to the film surface is changed from 0° to 90° by 15° steps. Moreover, activation (pinning) energy values of the film studied are found using thermally activated flux creep model when flux pinning force is analyzed by Kramer equation. It is found that the superconducting properties of the Bi-2223 superconducting film, the surface of which is centrally distributed and comprised of disproportionate number of peaks, decrease systematically with the increment of both the applied magnetic field and the angle up to 90° ($\mu_0 H//c$-axis). To sum up, the pinning mechanism and superconducting

iv

properties are strongly dependent upon both the applied magnetic field and the angle (ϕ), presenting the anisotropic character of the sample produced.

ÖZET

SAÇILMA YÖNTEMİ İLE ÜRETİLEN Bi(Pb)SrCaCuO SÜPERİLETKEN İNCE FİLMİN ELEKTRİKSEL VE MAGNETİK ÖZELLİKLERİ

YILDIRIM, Gürcan

Doktora, Fizik Bölümü

Tez Danışmanı: Prof. Dr. Ahmet VARİLCİ

Yardımcı Tez Danışmanı: Doc. Dr. Cabir TERZİOĞLU

Ekim 2012, 102 Sayfa

Bu tezin ana konusu sadece Bi(Pb)SrCaCuO süperiletken ince film üretimi için sadece ideal tavlama ortamını belirlemek değil aynı zamanda 100 watt'lık DC güçte saçılma metodu ile üretilmiş filmlerin teknoloji ve endüstri uygulamaları için elektriksel, fiziksel, mikro yapısal, çivileme mekanizmasını ve süperiletken özelliklerini taramalı elektron mikroskobu (SEM), X-ışını kırınım analizi (XRD), elektron dağılımlı X-ışını (EDX), özdirenç ve kritik akım yoğunluğu ölçümleri vasıtasıyla incelemektir. İlk aşamada, literatür araştırmasından sonra, en iyi yüzey morfolojisine ve süperiletken özelliklere sahip Bi(Pb)SrCaCuO film üretebilmek için farklı tavlama süreleri (15 dakika, 1.5 saat ve 3 saat) ve tavlama sıcaklıkları (850, 860 ve 870°C) belirledik. Yukarıda verilen deneyler üretilen 9 film üzerinde gerçekleştirildi. Elde edilen deneysel sonuçlar, 860°C 3 saat tavlanan süperiletken

film en büyük Bi-2223 faz oranına, en yüksek kritik sıcaklığa, kritik akım yoğunluğuna, en iyi yapı, kristalleşme ve süperiletken tanecik arasındaki bağlantısına, en geniş parçacık boyutuna ve en düşük boşluğa ortaya koyduğunu gösterir. İkinci aşamada, 860°C de 3 saat tavlanan Bi-2223 ince filmin çivileme mekanizması ve süperiletken özellikleri 20 K'den 130 K'e değişen sıcaklığın bir fonksiyonu olarak 0-3 T aralığında farklı magnetik alan altında yapılan magneto özdirenç ölçümleri yardımıyla analiz edildi. Filimin başlangıç (T_c^{onset}) ve ofset (T_c^{offset}) kritik sıcaklıları, kritik sıcaklık değişimleri, aktivasyon enerjisi (U_0), tersinmezlik alanı ($\mu_0 H_{irr}$), üst kritik alanı ($\mu_0 H_{c2}$), nüfuz etme derinliği (λ) ve uyum uzunluğu (ξ) magneto özdirenç eğrilerinden belirlendi. Süperiletken özelliklerin, uygulanan magnetik alanın artmasıyla numunenin içindeki süperiletken tanecikler arası zayıf bağlantıların bir sonucu olarak bozulduğu bulundu. Son aşamada, üretilen Bi-2223 filmin anizotropik davranışını incelemek için atomik kuvvet mikroskobu (AFM), magnetik alan yönünün bir fonksiyonu olarak (dc magnetik alan ve film yüzeyi ile uygulanan magnetik alan arasındaki açı) magneto özdirenç ve kritik akım yoğunluğunu ölçümleri gerçekleştirildi. Film yüzeyi alan yönünde 0° den 90° ye 15° adımlarla değiştirildi. Ayrıca, çalışılan filmin aktivasyon (çivileme) enerji değerleri termal aktive akı akış modeli kullanılarak bulunurken akı çivileme kuvveti Kramer eşitliğinden analiz edildi. Yüzeyi merkezi olarak dağıtılmış ve tepe noktalarının aşırı miktarda oluşan Bi-2223 süperiletken filmin hem uygulanan magnetik alanın hem de açının 90°'ye kadar artmasıyla ($\mu_0 H$//c-axis) süperiletken özelliklerin sistematik olarak azaldığı bulundu. Sonuç olarak, çivileme mekanizmasını ve süperiletken özellikler ciddi bir şekilde hem uygulanan alana hem de açıya (ϕ) bağlıdır, bu da üretilen numunenin anizotropik karakterini gösterir.

Anahtar Kelimeler: Bi-2223 süperiletken ince film, Tavlama ortamı, Kritik sıcaklık, Kritik akım yoğunluğu, Aktivasyon enerjisi, İğneleme mekanizması, Anizotropik davranış.

This dissertation is devoted to my parents...

ACKNOWLEDGEMENTS

TABLE OF CONTENTS

LIST OF TABLES

xiv

LIST OF FIGURES

CHAPTER 1

1. INTRODUCTION

Superconductivity was first noticed by the resistance measurement of the liquid mercury in 1911 by the Dutch scientist Heike Kamerlingh Onnes [1]. When the mercury (Hg) was cooled to liquid Helium temperatures (4.2K), the resistance fell down to zero ohm ($R=0$ Ω) and no resistance value against current appears anymore. The phenomenon of superconductivity is observed in the electrical resistance vanishing at a finite temperature called the critical temperature and denoted T_c (Fig. 1.1). During the huge period, the superconductivity has held out appealing possibilities for widespread applications. However, low temperature at which the materials exhibit the superconducting properties, only a few kelvins above absolute zero (0 K), limits their applications in technology and industry and causes the formidable technical problems [2].
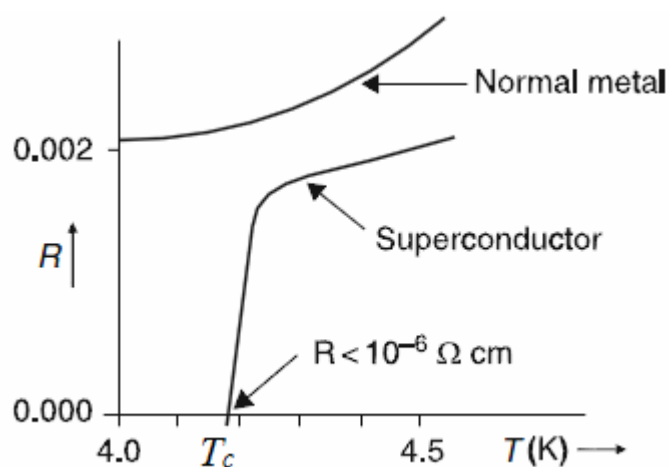
Figure 1. 1: Temperature dependence of resistance of a normal metal and a superconductor [2]

1

After a short time, it was found that a sufficient magnetic field (higher than critical magnetic field, μ_0H_c) generated from the current destroys the superconductivity of the material. The critical magnetic field was observed to be about a few tenths of tesla (*T*) for the elements such as lead and tin. Over many years, in 1933, Meissner and Ochsenfeld proposed another important discovery for the superconductivity. According to their experiment, when a superconducting material is cooled at the presence of the magnetic field applied, the magnetic flux is suddenly completely expelled from the interior of the material. This phenomenon is defined as Meissner effect [3] as shown in Figure 1.2.

Normal state   Superconductor state
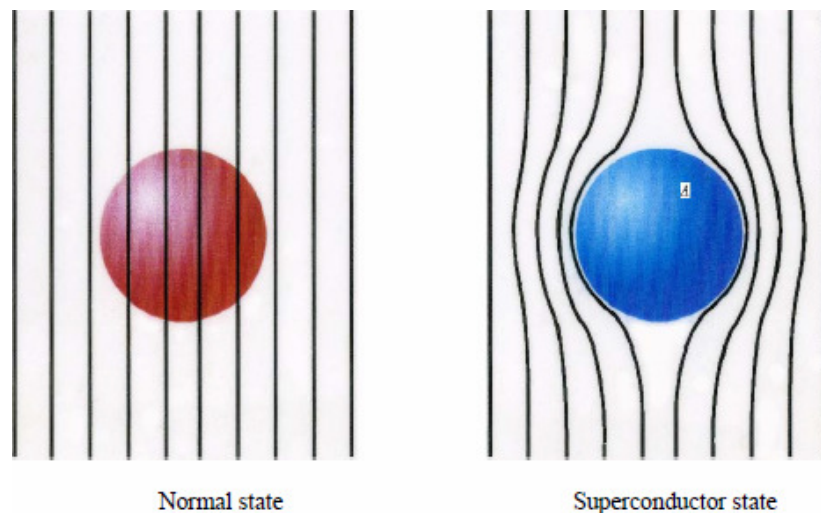
Figure 1. 2: Meissener effect in a superconducting sphere cooled in a constant applied magnetic field [4]

In other words, the superconductor exhibits perfect diamagnetism that is the ability of a superconductor to shield its interior from an applied magnetic field [4], meaning that the perfect diamagnetism is a fundamental property of the superconducting state. Superconductors in which the flux exclusives completely for any applied field less than the critical magnetic field are named as type I. On the

other hand, the flux penetrates totally above the critical value. Generally, elements or simple alloys are Type I superconductors (Fig. 1.3).
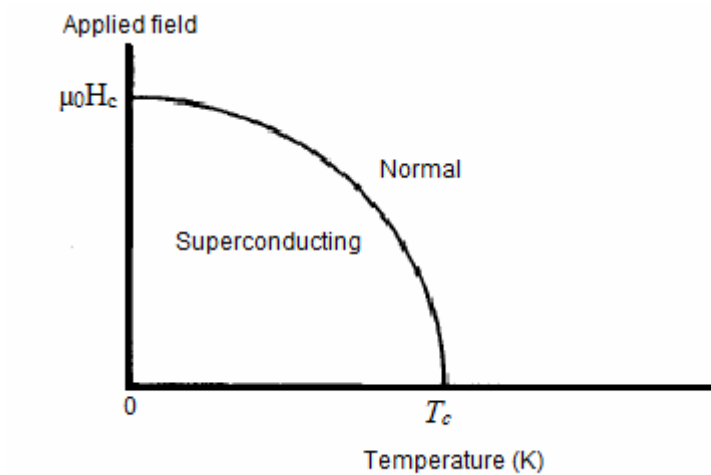
Figure 1. 3: Type I superconducting materials exhibit perfect diamagnetism up to a critical field $\mu_0 H_c$ [5]

On the other hand, for type II superconductors, magnetic flux penetrates into the material in the form of localized flux lines [5]. Each of the flux carries a single quantum of magnetic flux and the material exhibits the superconducting properties up to a value of magnetic flux ($\mu_0 H_{c2}$). When the flux starts to penetrate the material at $\mu_0 H_{irr}$, the material becomes normal over the value of $\mu_0 H_{c2}$ (Figure 1.4).

3
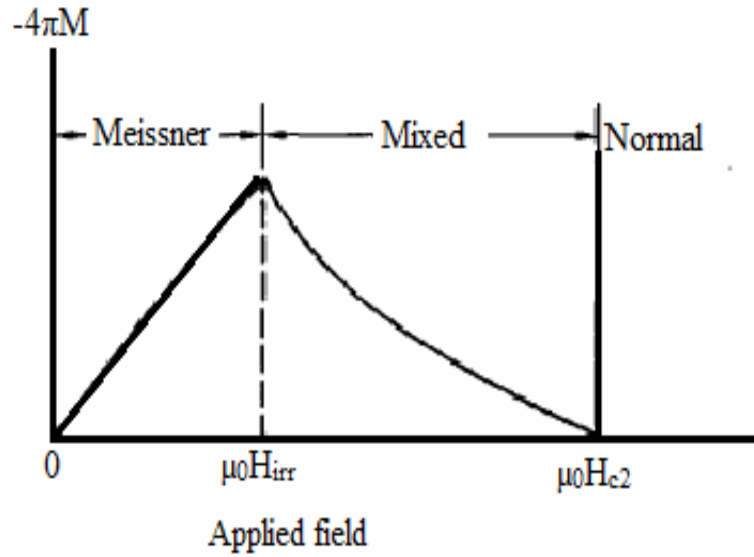
Figure 1. 4: Type II superconducting materials exhibit perfect diamagnetism up to a field $\mu_0 H_{irr}$, enter a mixed state between the field $\mu_0 H_{irr}$ and $\mu_0 H_{c2}$, then exhibit normal metal behavior above the field $\mu_0 H_{c2}$ [5]

In 1934, Gorter offered an important idea of a two-fluid model where the electron gas within the superconductor obtains two compounds. One of them carrying the super current has no entropy whereas the other compound behaving like a normal electron gas has all the entropy [6]. Furthermore, in this idea, the superconducting electrons short out the normal electrons below the superconducting transition temperature; hence, the electrical resistance for the material goes to zero. After a year, Fritz and Heinz London carried out an important theoretical analysis of the response of a superconductor in the presence of an applied magnetic field [7]. The theory showed that a bulk superconductor exhibits both perfect conductivity and diamagnetism. With the aid of the Maxwell's equations, both predict that the magnetic flux generated is excluded from all body expect for the surface region of the superconducting material. The decay of the field at the surface appears exponentially within a characteristic distance (penetration depth, λ).

4

At the beginning of 1950, there have been several advances in finding new and useful superconductors, leading to the production of type II superconducting materials because of the remarkable high transition temperature. The type II superconductors are characterized by means of the "mixed state" region where the magnetic flux penetrates partially while the bulk of the material maintains zero electrical resistance. Moreover, the type II superconductors remaining the superconducting properties up to their critical field values (generally 10 T or more) obtain greater critical transition temperature than the type I superconductors, confirming that the former is more useful than the latter in the technological and industrial applications. In that period, among the type II superconductors, A15 compounds such as Nb_3Sn and V_3Si obtain the critical transition temperatures of 18.5 K and 16.9 K, respectively. However, there was a limitation on commercial application for the inner material, thus the new material of Nb-Ti superseded the Nb_3Sn material as a result of the considerably more ductile structure. Especially, in the production of compact high field magnets operating up to several teslas, the Nb-Ti superconducting material has found widespread use in flourishing superconductivity industry.

In the middle of twentieth-century, the scientists tried to answer the question about how superconductivity appears at the microscopic level. A crucial step was carried out in 1956 when Leon Cooper proposed the important concept that superconductivity was related to a bound pair of electrons, each travelling through the lattice with equal but opposite spin and angular momentum. The pairs identified are bound by an electron-phonon interaction. According to this idea, in 1957 Bardeen, Cooper and Schrieffer (BCS) produced their famous theory where the superconductivity arises from the presence of the "Cooper pairs" mediated by the

electron-phonon interaction [8]. The description of Cooper pairs is quite enough to explain the mechanism of the conventional low temperature superconductors. Additionally, the BCS theory accounted for numerous experimental observations, such as the existence of an energy gap 2Δ (0) between the superconducting and normal electrons with a predicted value close to the absolute zero of 3.5 kT_c, and rapidly became firmly established [6]. Several experiments performed have confirmed the energy gap 2Δ (0) in the conventional superconductors. Furthermore, the penetration depth (λ) and the coherence length (ξ), being fundamental to superconductivity, emerge as natural consequences of the BCS theory.

1.1 Penetration Depth

As well known, the magnetic fields are expelled from the interior of the type I superconducting material as a result of the formation of surface currents. Although the currents are not formed in infinitesimally thin layer on the surface they slightly penetrate into the surface of the material ($\approx$100 nm). At the same time, the magnetic field (B) inside a type I superconductor exponentially reduces from its external value to zero with regard to the equations given below:

$$\nabla \times B = \frac{4\pi j}{c} \qquad \text{(Ampere's law)} \qquad (1)$$

London's second equation is manipulated by applying Ampere's law and Eq. 2 is obtained.

$$\nabla^2 B = \frac{1}{\lambda_L^2} B \text{ and where } \lambda_L = \sqrt{\frac{mc^2}{4\pi n_s e^2}} \qquad (2)$$

where λ_L denotes the characteristic length scale called as London penetration depth [9]. For a simple geometry, the solution inside the superconductor studied may be shown as:

$$B(x) = B_0 e^{-x/\lambda_L} \qquad (3)$$

The solution of the London equation presents that an applied magnetic field penetrating a little way into a superconductor falls off exponentially over a mean distance λ_L, named as the penetration depth that is typically less than 0.05 µm and it is not wrong to say that a macroscopic superconductor entirely excludes the applied magnetic fields. Based on the Eq. 3, the variation of the magnetic field inside a type I superconductor (semi-infinite) with respect to the distance can be displayed in Figure 1.5. As seen from the figure that the superconductor extends throughout the positive
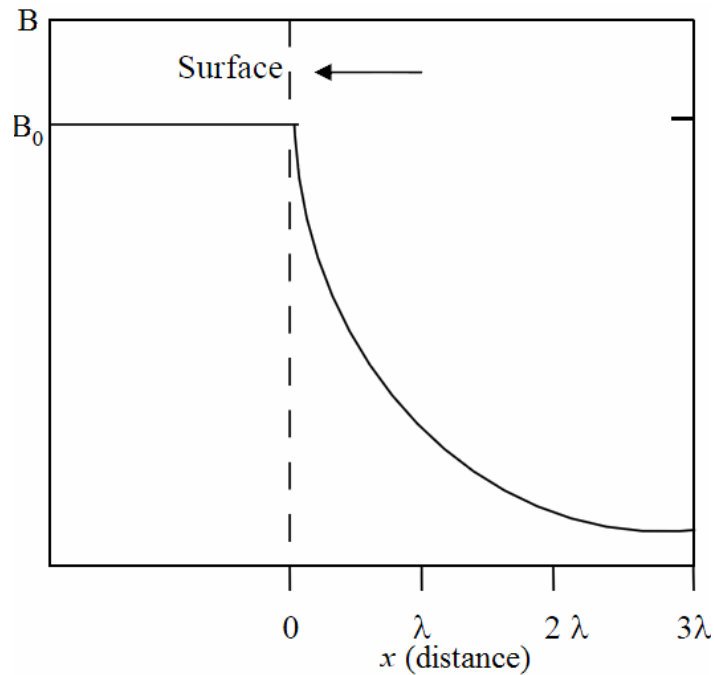
Figure 1. 5: The magnetic field, B, inside a superconductor (semi-infinite) against distance x from its surface. The field outside the superconductor (for $x<0$) is B_0, and the superconductor is to the right of the dashed line [4]

side of the x axis and the magnetic field applied becomes very small at a depth of a few times λ in the range of 10–100 nm below the surface. However, the penetration depth values of the material vary with temperature according to empirical expression:

$$\lambda(T) = \lambda_0 \left[1 - (T/T_c)^2 \right]^{-\frac{1}{2}} \qquad (4)$$

where T_c denotes the critical transition temperature of a superconducting material when λ_0 is the penetration depth at T = 0K [10].

1.2 Coherence Length

Coherence length is the smallest dimension over which the electrons interact to form Cooper pairs, in other words, the superconductivity can be established or destroyed over the coherence length. The intrinsic coherence length (ξ_0) calculated from the Ginsburg–Landau model generally exceeds 0.3 µm in type I superconductors [11, 12]. For a pure metal, the actual coherence length is found to be about the same value; however, in alloys or impure compounds the ξ_0 value is obtained to be much smaller because of the fact that the mean free path for electrons is smaller. Type II superconducting metals are evaluated into this category, presenting that the superconducting properties of the material can be changed with the aid of the change of the electron mean free path, such as the introduction of the lattice defects.

Moreover, it is well known that the applied magnetic field penetrates into the type-II superconductor in the form of vortices. Each vortex carries a flux quantum $\Phi = h/2e$, and consists of both a cylindrical core of a radius ξ (called as coherence length) and a current circulating around the core out to a distance λ (named as penetration depth of the material).

Further, the ratio between the penetration depth and coherence length, being called as Ginsburg–Landau ratio, is important parameter to decide the type of the superconductor. For convenience of categorizing superconductors, the Ginsburg–Landau ratio is defined as the following equation [13],

8

$$(\kappa = \lambda / \xi_0) \tag{5}$$

For the type I superconductors, the coherence length observed is found to be larger than the penetration depth ($\kappa < 1$). For the type II superconductor, the Ginsburg–Landau ratio is reversed ($\kappa \square 1$). In fact, the breakpoint for the ration is found to be at $\kappa \approx 0.707$. Figure 1.6 gives the comparison of in type I and type II superconductors. It is apparent from the figure that for the type I, any magnetic field does not penetrate far enough to affect the electrons within a coherence length; on the other hand, for type II material, superconductivity which can still live with a nearby magnetic field penetrating into the material is confined to within such a short coherence length.
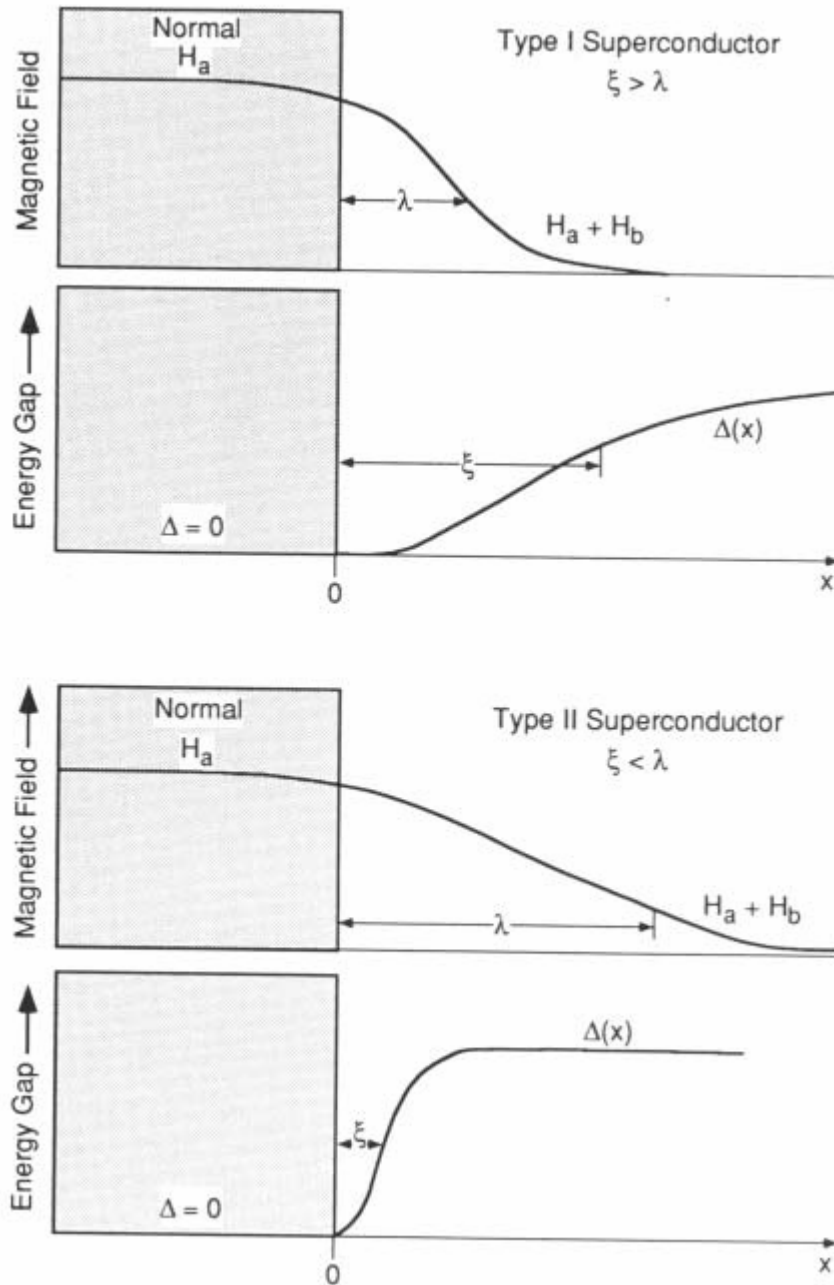
Figure 1. 6: The applied magnetic field and energy band gap parameter $\Delta(x)$ at the boundary between superconducting and normal regions for both type I and type II superconducting materials. The differences obtained stem from differences in the penetration depth and coherence length [13]

Gavaler produced a stoichiometric film of Nb_3Ge with superconducting transition temperature of 23.1K (above the normal boiling point of liquid hydrogen) in 1973. In the following years, a large number of researchers tried to produce superconducting materials with higher transition temperatures; however, all attempts

were unsuccessful and this gave rise to the widely held belief that superconductivity was restricted to low temperatures and would be unlikely to appear much above 25 K [14]. The BCS theory showed that the maximum critical temperature was around 30-35 K. Fortunately, a number of scientists have continued their studies to obtain superconductor samples in liquid nitrogen temperature for years.

1.3 Type-II superconductors

In the middle of the 1980s, Georg Bednorz and Alex Muller (1986), from IBM Zurich laboratories, submitted an innocuous looking paper to the journal Zeitschrift für Physik. With the aid of this paper submitted, one of the most exciting periods ever in condensed matter physics started. The paper pointed out that the compound of *La-Ba-Cu-O* including the barium oxide and cupper oxide obtains the higher critical temperature of about 35 K [15]. Only one year later, yttrium oxide was substituted by lanthanum oxide in the system and a new compound, *Y-Ba-Cu-O*, was discovered. Surprisingly, the critical temperature of this new compound was found to be over 90 K [16] and the superconductivity at liquid nitrogen temperature (77K) was not a dream. This discovery accelerated the research efforts to discover new compounds with higher T_c. In the same year, the superconductivity in *Bi-Sr-Cu-O* system was found by Michael et al. [17]. In the year after 1986, calcium (Ca) was added into this system by Maeda et al. [18] and the superconductivity was observed at 105 K for the new system called as high temperature superconductor. However, this system with the addition of lead (Pb) exhibited the superconductivity at 110 K [19]. Figure 1.7 demonstrates that how the maximum critical transition temperature has changed as a function of time, presenting the dramatic increase stemming from the international scientific response to the discovery of the high-T_c materials [20].
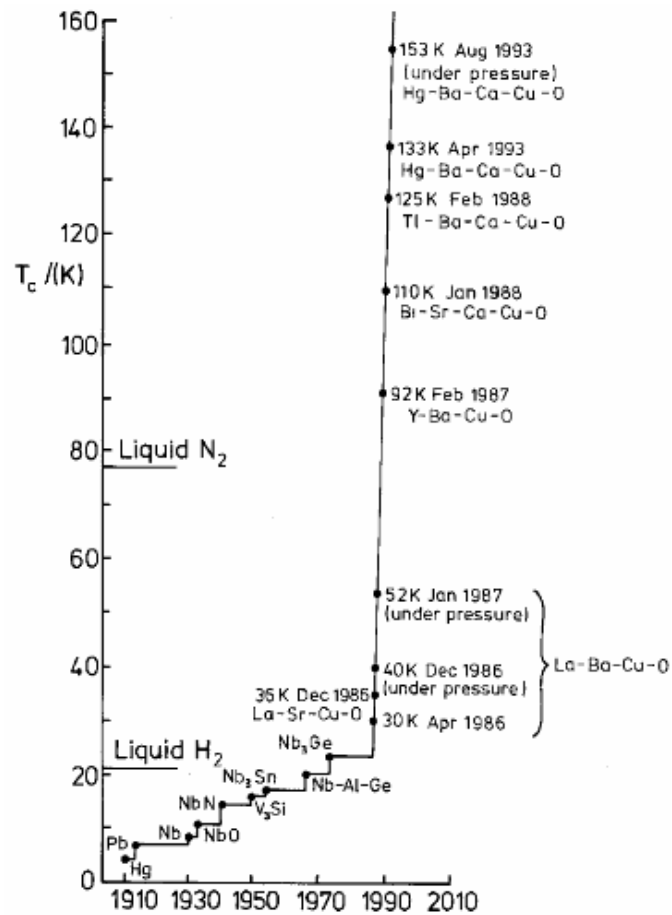
Figure 1. 7: The historical development of superconductivity

With the discovery of Bi–Sr–Ca–Cu–O (BSCCO) high temperature superconductors in 1988 [1], the interest in both the fundamental research and applications in technology and industry of these materials has been increased day by day owing to their remarkable high transition temperature, smaller power losses, high current and magnetic field carrying capacity, optical and electronic properties [21–27]. The BSCCO system obtaining a layered structure has three different phases with regard to its chemical compositions, the Bi-2201 phase ($n = 1$, $T_c \approx 20$ K), the Bi-2212 phase ($n = 2$, $T_c \approx 85$ K) and the Bi-2223 phase ($n = 3$, $T_c \approx 110$ K) [28].

1.4 Crystal Structure of the $Bi_2Sr_2CuO_6$ (Bi-2201) System

$Bi_2Sr_2CuO_6$ (2201) compound discovered by Michel et al. in 1987 obtains the lowest T_c (0-20 K) among the Bi-based superconductors and has a tetragonal symmetry with lattice parameters $a = b = 5.39$ Å, $c = 24.6$ Å [29].

Unit cell of $Bi_2Sr_2CuO_6$ is shown in Figure 1.8 [30]. As seen from the figure that along the c axis the block consisting of two Sr-O and one Cu-O layers repeat itself with a translation of $a/2$, $a/2$ in the xy plane and form the unit cell. Besides, the bases are Bi-O layers and copper atoms form an octahedral structure with the closest 6 oxygen atoms in the crystal structure.
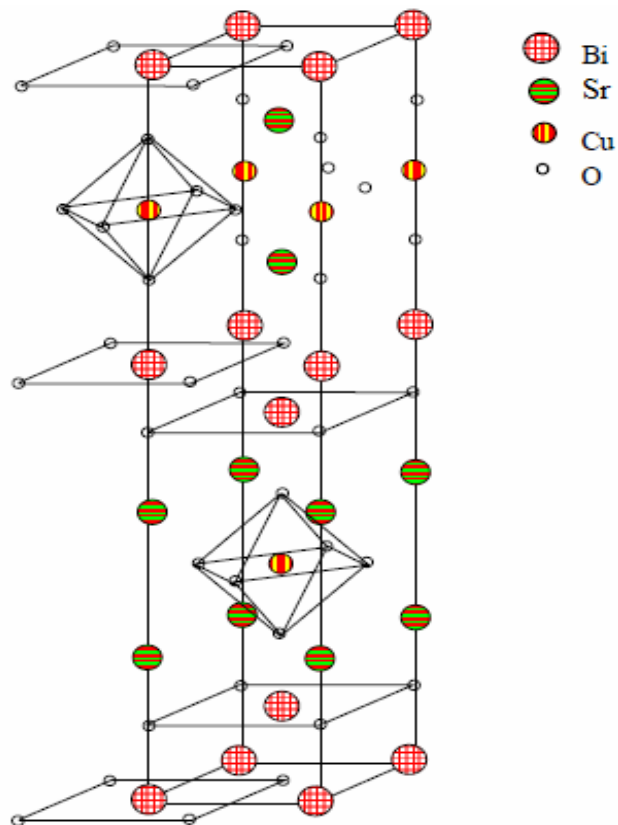
Figure 1. 8: Crystal structure of $Bi_2Sr_2CuO_6$ compounds [4]

1.4.1 Crystal Structure of the $Bi_2Sr_2CaCu_2O_8$ (Bi-2212) System

Maeda et al. discovered $Bi_2Sr_2CaCu_2O_8$ (2212) compound by adding the Ca into $Bi_2Sr_2CuO_6$ system in 1988. Its crystal structure is pseudo-tetragonal with lattice parameters a = b= 5.4 Å, and c = 30.6 Å. Critical transition temperature is observed to change from 75 to 85 K [29] with regard to the purity and preparation conditions. Figure 1.9 depicts the crystal structure of $Bi_2Sr_2CaCu_2O_8$ compounds [30]. It is obvious from the figure that the Bi-2212 system is composed of Bi-O layers in the bases and two Sr-O layers, two Cu-O layers and one Ca layer. The copper atoms form an octahedral structure with 6 oxygen atoms in 2201 compound and pyramid structure with 5 oxygen atoms in 2212 compound, respectively. However, the Ca atoms are embedded without oxygen bound along the ab plane between the Cu-O pyramids.
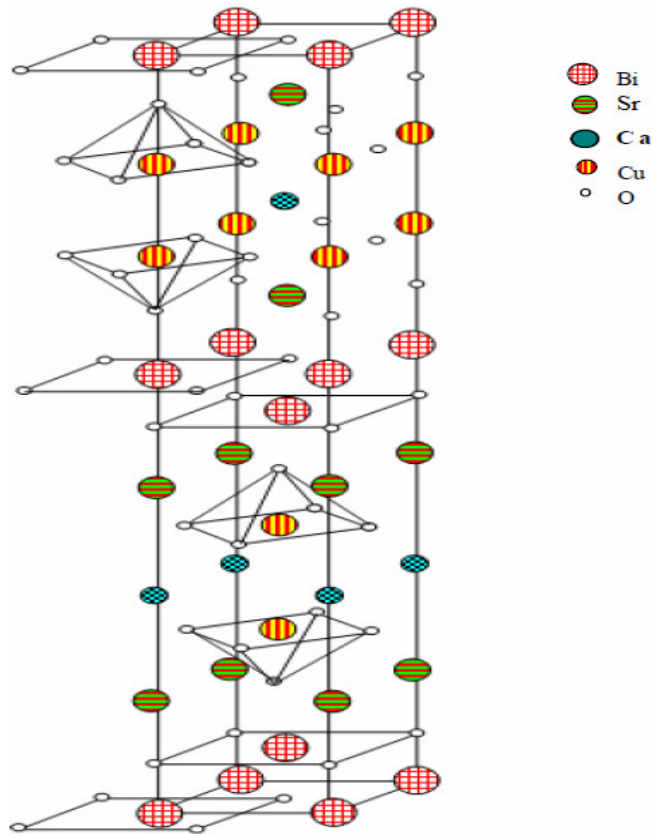
Figure 1. 9: Crystal structure of $Bi_2Sr_2CaCu_2O_8$ compounds [4]

14

1.4.2 Crystal Structure of the $Bi_2Sr_2Ca_2Cu_3O_{10}$ (Bi-2223) System

In the Bi-based superconducting ceramic series, the $Bi_2Sr_2Ca_2Cu_3O_{10}$ (2223) compound has the highest critical transition temperature of 110 K and is in the form of pseudo-tetragonal structure. Figure 1.10 illustrates the crystal structure of Bi-2223 phase [30]. One can see from the figure that the Bi-2223 system consisting of two Bi-O layers, two Sr-O layers, two Ca and three Cu-O layers [31] is formed via the addition of both Ca and Cu-O2 layer into the Bi-2212 crystal structure; hence, the cell parameter c enhances to 37.1 Å. In addition to the pyramid structure, the copper atoms form square layers with 4 oxygen atoms (See Figure 1.10).
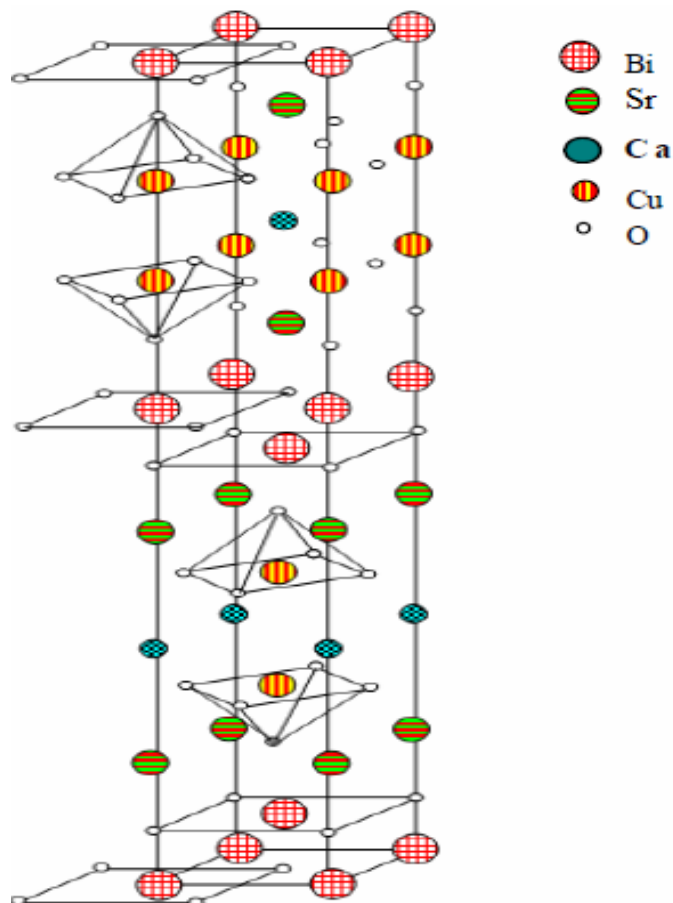
Figure 1. 10: Crystal structure of $Bi_2Sr_2Ca_2Cu_3O_{10}$ compounds [4]

Among the Bi-based superconductors, the double layered cuprate (Bi-2212) is superior to the Bi-2201 because of the fact that its oxygen stoichiometry is relatively invariant with regard to cationic addition when the samples are produced in an identical thermal environment [32]. Furthermore, the Bi-2212 superconductors have lesser weak link problems compared to Bi-2223 superconductors and are suitable for the preparation of long wires and tapes with high critical current densities (J_c). However, as received the applied magnetic fields and high temperatures limit their applications due to the significant reduction in condensation energy density, strong anisotropic properties, extremely short coherence length (ξ), and large penetration depth (λ) [28]. Likewise, according to the many researches [33, 34], the Bi-2212 superconductors have relatively poor mechanical properties, limiting the use of these materials in most of practical applications. On the other hand, in these series, the Bi-2223 phase is the most attractive owing to the highest critical temperature (T_c) of about 110 K [35, 36]. Nevertheless, the preparation of the Bi-2223 phase is a very difficult task due to the high complexity of the reaction and the appearance of numerous phases as Bi-2212 and Ca_2PbO_4 during the phase formation [37]. Several preparation conditions such as the annealing ambient (time, temperature, atmosphere and pressure), composition, type and quantity of the dopant, heat-treatment method and operational procedures also affect the formation of Bi-2223 phase. In particular, the annealing ambient plays a very significant role on the phase fabrication of the high-T_c cuprate superconductors due to the electron–phonon anharmonicity [38]. In this respect, it is necessary to produce the superconductors with higher T_c in the form of high quality thin films on a suitable substrate under convenient ambient conditions for numerous technological applications such as microwave integrated circuits, high-frequency devices, magnetic shielding devices and resonators [39]. In order to

prepare high quality thin film superconductors, several techniques such as molecular beam epitaxy [40], laser ablation [41], the excimer laser etching [42], coevaporation [43], in situ single chamber arc sputtering [44], ion beam sputtering [45], chemical vapor deposition [46] and magnetron sputtering [47] have been experienced.

Additionally, many researchers have endeavored to improve the electrical, superconducting, mechanical, microstructural and flux pinning properties of the thin film superconductors to make them suitable for high temperature and magnetic field applications [48–55]. As well known, both high critical temperature and high critical current density are necessary for usage of the Bi-2223 films in the electronic applications. J_c can be enhanced by creating pinning centers in the superconductor sample. The interaction between flux lines and pinning centers leads to high J_c [56]. For this reason, low anisotropy of the sample under magnetic field plays a crucial role in understanding the phenomenology of high temperature superconductors (HTSCs). The flux pinning and the grain alignment are two main factors that determine the critical current density. Dependence of resistivity, J_c and μ_0H_c on the angle between external magnetic field and c-axis of the superconducting sample can be used to gather information on the flux pinning and grain alignments in the sample. However, bulk HTSC samples contain grains oriented in different directions, so it is difficult to perform such angle dependent studies on them. These investigations have been carried out on epitaxial HTSC films [57]. Yamasaki et al. [58] investigated the angle dependence of J_c for Bi-2223 films. They found that anisotropic J_c behavior of the Bi-2223 films is intrinsic. Depending on the direction of the field applied on the surface of the film, one can learn whether the CuO_2 planes decouple or not and there is dissipation related to the flux flow or not [59]. Moreover, Oota et al. [60] reported that the J_c value in a tilted field is dominated only by the field component parallel to

17

the c-axis, independent of the in-plane component and similar results have been observed for the Bi-2212 thin film [61].

This dissertation is organized as follows. Chapter 2 presents thin film deposition techniques clearly. Sample preparation and measurement techniques of this investigation are outlined in Chapter 3. Results and discussions are displayed in Chapter 4. Final chapter includes conclusions obtained.

CHAPTER 2

2. THIN FILM DEPOSITION TECHNIQUES

Typical deposition techniques are examined on two broad categories with regard to the process applied: chemical or physical [62].

2.1 Chemical vapor deposition (CVD) processes

Chemical deposition process of the films and coatings involve the chemical reactions due to the gaseous reactants on or near the vicinity of a substrate surface heated. Therefore, the volatile materials (gaseous reactants) are atomistically deposited to produce a nonvolatile solid on a crystalline substrate [63–65]. With the aid of the atomistic deposition method, not only are highly pure materials with structural control at atomic or nanometer scale level produced for the potential technological (especially microelectronics devices) and industrial applications [66–70] but the single layer, multilayer, composite, nanostructured, and functionally graded coating materials with well controlled dimension and unique structure at low processing temperatures are fabricated for numerous technological applications such as microwave integrated circuits, high-frequency devices, magnetic shielding devices and resonators [71–76].

Chemical deposition processes can be further categorized by the phase of the precursor:

2.1.1 Plating deposition

In this method, the liquid precursors are composed of a water solution with a salt of the deposition metal. Although the most commercially important process is electroplating, the reagents in the solution prepared for noble metals play the vital role on the process [77].

2.1.2 Chemical solution deposition (CSD)

In this technique, also known as sol-gel method, a liquid precursor contains a solution of organometallic powders dissolved in an organic solvent. Many research groups have nowadays preferred this chemical deposition method for fabrication of the thin film due to the relatively inexpensive and simple preparation [78–80]. Besides, this deposition process is able to produce stoichiometrically accurate crystalline phases [81, 82].

2.1.3 Spin Coating (SC)

In this method, a liquid (sol-gel) precursor is deposited onto a smooth, flat substrate, being subsequently spun at a high velocity to centrifugally spread the solution over the substrate. According to the viscosity of the sol and the speed of the substrate, the ultimate thickness of the deposited film is determined. Additionally, the thickness of film prepared can be increased by the repeated depositions; however, the film produced should be exposed to the annealing process for the crystallization of the amorphous spin coated film so that the film exhibits certain preferred orientations on single crystal substrates [83]. For several years, this technique has

widely been used to fabricate the thin film for the technological and industrial applications [84–88].

2.1.4 Atomic layer deposition (ALD)

In this method, gaseous precursor is used for the deposition of the thin film at low temperatures compared to the CVD method. The deposition carried out into two half reactions is run in sequence and repeated for each layer to ensure total layer saturation before the production of the next layer on the single crystal substrate; hence, the reactants are sequentially deposited on the substrate [89–91]. However, it is a disadvantage that the process conducted is really slower than CVD [92, 93].

2.2 Physical Vapor Deposition (PVD)

In these processes, a thin film of solid is produced by means of the mechanical or electromechanical systems in a vacuum deposition chamber to allow the particles to travel as freely as possible so that the particles follow a straight path and reach the crystal substrate without reacting with or scattering against other gas-phase atoms, leading to reduce the incorporation of impurities from the residual gas in the vacuum chamber [94]. Physical deposition processes can be further categorized by the phase of the precursor:

2.2.1 Pulsed laser deposition

In this method, the film deposition is based on an ablation process. The emitted pulses of the laser light are focused on the surface of target to vaporize the

materials and generate the plasma, reverting (usually) to a dense gas-particle flow before it reaches the substrate [95].

2.2.2 Cathodic arc deposition

This technique uses a high current but low-voltage arc to vaporize a cathodic electrode (called as cathodic arc) or anodic electrode (defined as anodic arc) and to deposit the particles (vaporized by highly ionized source) on a substrate [96]. In other words, in the cathodic arc deposition, the electrical arc is created by means of the high current generated by the blasts ions from the cathode. Further, when a reactive gas is entered into the system during the evaporation process, the film fabrication process can be shortened as a result of dissociation, ionization and excitation.

2.2.3 Electrohydrodynamic deposition

This method is a relatively new process for the thin film deposition in which the liquid film can be produced on the substrate either in the form of nano-particle solution or simply a solution with the use of a high power source. During the evaporation process, the crystal substrate is connected to the ground terminal of the power source. At the same time, the uniform thin layer is observed on the substrate due to the influence of electric field.

2.2.4 Evaporation

In this method, metal is melted in high vacuum and transported to the substrate; hence the deposition rate depends strongly on the pressure, temperature and molecular weight of the species. The two types of evaporation method are popular: thermal evaporation (heating by resistive elements or inductive heating) and (II) E-beam evaporation.

2.2.4.1 Thermal evaporation

In this method, an electric resistance heater is used to melt the material and raise its vapor pressure to a useful range in a very high vacuum. Hence, the deposition is performed without contamination of the film. The thermal evaporator comprises the evaporation of the source materials in a high vacuum chamber and so the evaporated particles are condensed on the substrates. This method is useful to produce the permeation barrier films on flexible packaging materials, electrically conducting films, and especially the optical interference, wear resistant, corrosion protective, mirror and decorative coatings [96]. Electron beam evaporator (EBE) and molecular beam epitaxy (MBE) are sophisticated form of thermal evaporation [97].

2.2.4.2 Electron beam evaporation (EBE)

For the refractory metals, this deposition process is used to evaporate particles due to the high melting point of the materials studied [98]. Moreover, in this method, the film deposition is conducted by a high-energy beam emitted from an electron beam evaporator to break off a small spot of material in a high vacuum.

The quality of the film deposited on the crystal substrate is fair to use in the technological applications [99, 100].

2.2.5 Molecular beam epitaxy (MBE)

This method performed in ultra-high vacuum at very low deposition rates is very well-controlled by thermal or electron beam sources at low temperature. Besides, in the MBE technique, the slow streams of a material can directly be sent to the substrate to deposit one atomic layer at a time [101, 102].

2.2.6 Sputtering

This technique that is the primary alternative to evaporation method provides better step coverage at much lower temperature than the latter one. Not only is less radiation damage observed compared to the EBE method but the stoichiometry control is better for multi-component systems, as well. At the same time, the sputtering process uses the plasma generated by the noble gas (sputtering gas, such as argon) to break off the particles from a target at low temperature, making this process be one of the most flexible deposition techniques. Moreover, fast and thickness control supply the advantage of the usage in the optical media. In particular, CD, DVD, and BD are at the heads of them.

The convenience sputtering processes are divided into four major categories: namely, DC, RF and magnetron (both DC and RF). The efficiency of DC and RF processes increases significantly by means of the magnetron sputtering.

2.2.6.1 DC sputtering

This method is called as diode or cathodic sputtering. Sputter voltage, current, substrate bias and pressure are important parameter for particle energy and relative film deposition rate. At low pressures, the cathode sheath gets wide and the ions start to be generated from the target. Thus, the mean free electron path between the collisions becomes larger and larger, and the electrons collected by the anode are not replenished by ion impact-induced secondary-electron emission at the cathode [103, 104]. Hence, ionization efficiencies start to decrease and self-sustained discharges cannot be maintained below the certain pressure (about 10 mtorr), leading to both the increment of the pressure at a fixed voltage and reduction of the electron mean free path. As a result, larger currents flow towards the crystal substrate due to the more ions generated. In case of the high pressure, the sputtered atoms are subjected to the increased collusion scattering and are not efficiently deposited. During the DC sputtering the atoms leaving the target with typical energies in a range of 5-50 eV undergo gas scattering events in passing through the plasma gas at low operating pressures. The atoms released from the target eventually reach the kinetic energy of the surrounding gas (at the mean distance from the cathode) as a result of the repeated energy-reducing collisions and the sputtered atoms become thermalized. The initial excess kinetic energy providing the bombardment of the depositing film starts to dissipate, resulting in the diffusion randomly. Not only is there a decrement in the number of the deposited atoms but there is also little compaction or modification of the resulting film structure [104].

2.2.6.2 AC (RF) sputtering

Similar to DC sputtering, this method being a different technique of the generating ions avoids charge build-up by alternating potential. The sign of the anode-cathode bias is varied at a high rate and when the target electrode is negative, the sputter deposition carried out. Hence, the RF sputtering works well to fabricate highly insulating oxide films [105, 106].

2.2.6.3 Magnetron Sputtering

This method is the most widely used variant of DC sputtering [107, 108] because of the higher deposition rates with lower voltage operation at low pressures. At typical pressures of a few millitorr for the magnetron sputtering, the particles sputtered fly off in ballistic fashion to impinge on the crystal substrates. On the other hand, the gas phase collisions and scattering at high pressures are avoided due to the randomization of the directional character of the sputtered particle flux and lower the deposition rate [109].

CHAPTER 3

3. EXPERIMENTAL DETAILS

3.1 Preparation of the $Bi_2Pb_1Sr_2Ca_{2.2}Cu_{3.2}O_y$ target

The starting materials are commercially available powders of PbO, SrCO$_3$, Bi$_2$O$_3$, CaCO$_3$, (Alfa Aesar Co., Ltd. 99.99% purity). Superconducting Bi$_2$Pb$_1$Sr$_2$Ca$_{2.2}$Cu$_{3.2}$O$_y$ material for the target is prepared by the standard solid–state reaction method [110, 111]. These oxides and carbonates are weighted in stoichiometric proportion with a precision microbalance (Fig. 3.1).
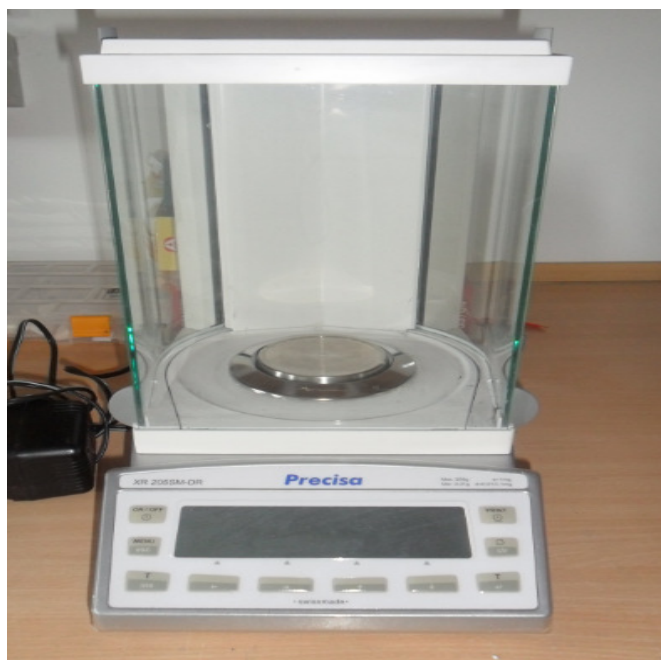
Figure 3. 1: XR 205SM-DR Precisa balance

The following balancing equation is used to determine the appropriate amounts of the powders.

Chemical equation:
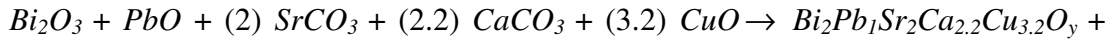
$Bi_2O_3 + PbO + (2) \ SrCO_3 + (2.2) \ CaCO_3 + (3.2) \ CuO \rightarrow Bi_2Pb_1Sr_2Ca_{2.2}Cu_{3.2}O_y +$ Gasses

COMPOUNDS	ATOMIC WEIGHT
Bi_2O_3	465.96
PbO	223.19
$SrCO_3$	147.63
$CaCO_3$	56.08
CuO	79.54

Table 3. 1: Molecular weight of the powders used in this work

Then, the powders are mixed in a grinding machine (Figure 3.2) for 24 h with a rotation speed of 2000 rpm in 10 min in a medium of atmospheric air to obtain homogeneous mixture.
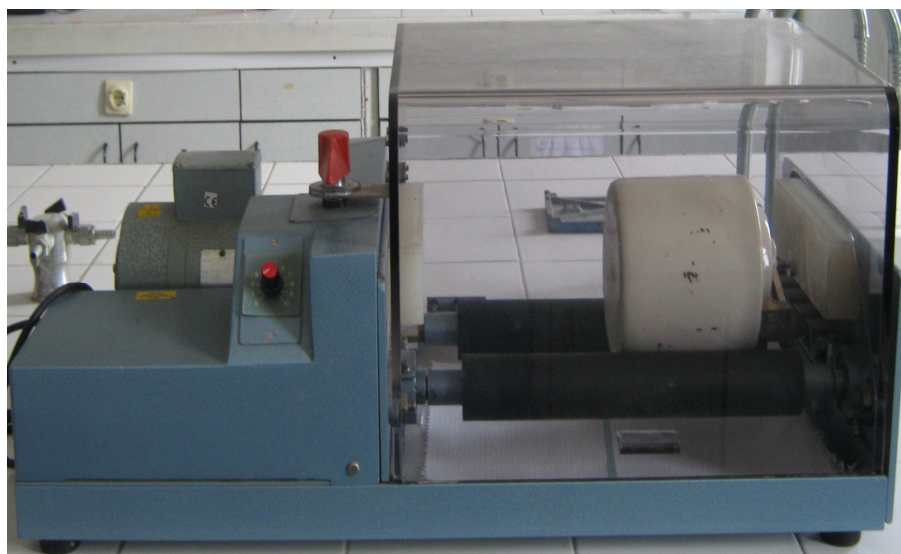
Figure 3. 2: Grinding machine

After milling process, the homogeneous mixture of powders is subjected to the calcination process in air at 800 °C for a period of 12 h (5 K per minute heating rate). As well known, the calcination process performed at lower temperatures than sintering process helps the carbons in the starting powders to release. When preparing the superconducting sample, this process plays vital role to rescue from the formation of the impurity phases. The final material calcined is reground and pressed into cylindrical bar of 50 mm in diameter and 5 mm in thickness at 225 MPa with a manual hydraulic press (Figure 3.3) to form a bulk target.

Figure 3. 3: TSEK TÜMAS manual hydraulic press

The target prepared is sintered at 845 °C for 12 h and then carefully stuck on the DC gun via the mixture of Aremco-bond 556-B Base and 556-A Activator obtained from Aremco products, inc. The sputtering system where the free electrons are accelerated away from the negatively charged electrode defined as cathode,

includes the sputter coater, rotary pomp, personal computer, nitrogenous and argon tubes (Figure 3.4).

Figure 3. 4: NSC-3000 sputter coater nano-master, Inc

The electrons accelerated collide with the outer shell electrons of the neutral (sputtering) gas atoms (99.999% pure argon) in their path. Outer shell electrons of the argon gas begin to fly out and the gas atoms are ionized. Hence, the positively charged ions (Ar^+) accelerated towards to the cathode and strike the target. Now, it is time to eject the electrons for the target. The electrons ejected from the target return to a ground state of the argon gas due to the conservation of energy law, and so the resultant neutral gas atoms gain energy. However, after a short period the argon releases the energy in the form of a photon, called as the plasma [112]. The schematic diagram of the process given above is depicted in Figure 3.5 in detailed.

Figure 3. 5 schematic:

Sputtering Target ($Bi_2Pb_1Sr_2Ca_{2.2}Cu_{3.2}O_y$)

Ar^+

Sputtering Gas

MgO (*100*) Substrate and film deposition
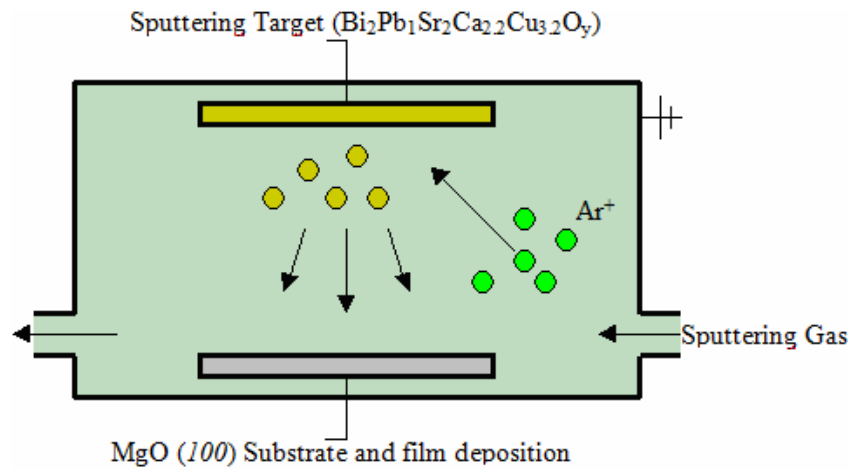
Figure 3. 5: Schematic diagram of the DC sputter

3.2 Substrate cleaning process

Prior to the film deposition process, all the MgO(100) single crystal substrates with dimensions of 10x5x0.5 mm^3 for production of the superconducting thin film are ultrasonically cleaned by acetone for ten minutes in trassonic 460/H ultrasonic cleaning unit (Figure 3.6), rinsed thoroughly with deionized water and blown dry in nitrogen flow, respectively. Thus, the crystal substrates are ready for the sputtering process.

Figure 3. 6: Trassonic 460/H ultrasonic cleaning unit

31

3.3 Film deposition process

When the $Bi_2Pb_1Sr_2Ca_{2.2}Cu_{3.2}O_y$ material with a 50 mm in diameter and a 5 mm in thickness is used as sputtering target, the substrates prepared are vertically placed onto the substrate holder (plate) and the distance between them is adjusted to be about 40 mm. The chamber is evacuated with the aid of rotary and turbo pump down to 6.33×10^{-6} torr, then 100 W DC power is applied between the target and plate for 3 hours in 99.999% pure argon (30 sscm for sputtering gas) atmosphere at room temperature. Nevertheless, the pressure is noticed to be nearly 5.04×10^{-3} torr during film sputtering process. At the end of the sputtering process, the chamber is vented by means of 99.99% pure nitrogen gas. Moreover, all the films produced are seen to be light darkish.

3.4 Film sintering process

Sintering is a technique to produce objects from the chemical powders and can be defined as: when a material is heated the below its melting temperature point (solid state sintering), its particles adhere to each other. This method is traditionally used to fabricate the ceramic objects. Especially, the sintering temperature is charge of the superconducting properties (critical transition temperature and critical current density) of type-II superconductors. Namely, at the optimum sintering temperature, the material studied obtains the larger grain size, being attributed to the higher critical temperature value of the material. Additionally, the critical current density enhances with the increment of the temperature and reaches its maximum value at a certain sintering temperature just below the temperature where the material starts to melt. However, the superconducting properties may sometimes destroy as a

consequence of the degradation of the pinning ability, density, crystallinity and connectivity between grains.

The $Bi_2Sr_2Ca_{n-1}Cu_nO_y$ system obtaining a layered structure has three different phases with regard to its chemical compositions. It is found that the optimum sintering temperatures of these three phases are about 820 °C for the Bi-2201 phase (n = 1, $T_c \approx 20$ K), 850–860 °C for the Bi-2212 phase (n = 2, $T_c \approx 85$ K), and 870 °C for the Bi-2223 phase (n = 3, $T_c \approx 110$ K) [113, 114] without any Pb doping in the systems. On the other hand, the optimum sintering temperature of the Pb-doped Bi-2223 system changes with regard to the addition level. If the sintering temperature is higher than optimum one, different phases such as the Bi-2212 phase, Ca_2CuO_3 can be detected in the system. In fact semiconducting-like R-T curves might also be observed because of the liquid layer forms in some regions of the grain boundaries [115, 116].

Optimum sintering time is another important parameter to obtain more uniform surface appearance, better texturing, crystallinity and connectivity between grains, leading to the increment in the superconducting properties of the material. If the sintering duration applied is shorter than the optimum one, variation of transition temperature (extracted from the resistivity curves) broadens, confirming the enhancement of the weak links between the superconducting grains [117]. Likewise, the longer sintering time may suppress the superconducting properties due to the loss of the volatile elements such as Pb, Cu and especially O.
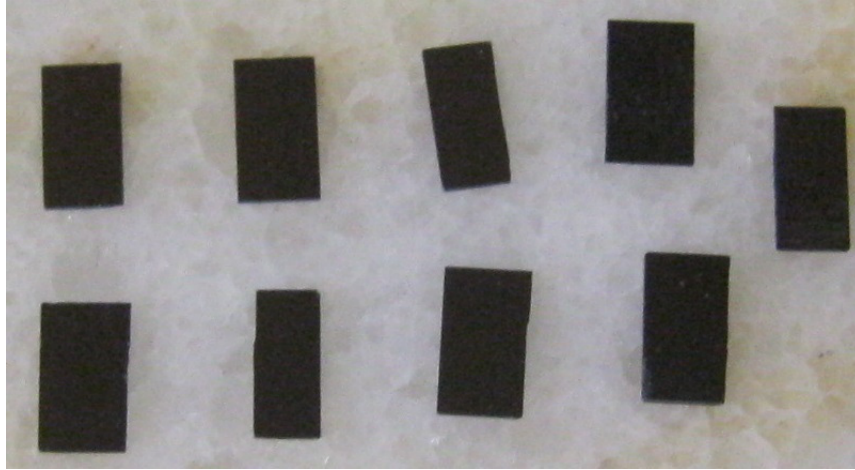
Figure 3. 7: BSCCO thin films produced in this work

In order to determine the optimum sintering ambient (temperature and time), 9 different samples (Figure 3.7) are produced using various temperature (850 °C, 860 °C and 870 °C) and time (15 min, 1.5 h and 3 h) in air atmosphere. Namely, the sintering process includes three main steps. In the first step, they are sintered at 700 °C for 1 h in the furnace with 5 °C per minute heating rate. In the second step, the samples prepared are annealed at 850 °C, 860 °C and 870 °C for different times (15 min, 1.5 h and 3 h) with 1 °C per minute heating rate and then cooled down to 720 °C with 5 °C per minute cooling rate, respectively. In the last step, all the films are suddenly took from the furnaces and cooled down to the room temperature in the air atmosphere. All the annealing processes are given in Figure 3.8 clearly. The calcinations and sintering processes of the films are conducted using the programmable furnace (PROTHERM-Model PTF12/75/200) (Figure 3.9).
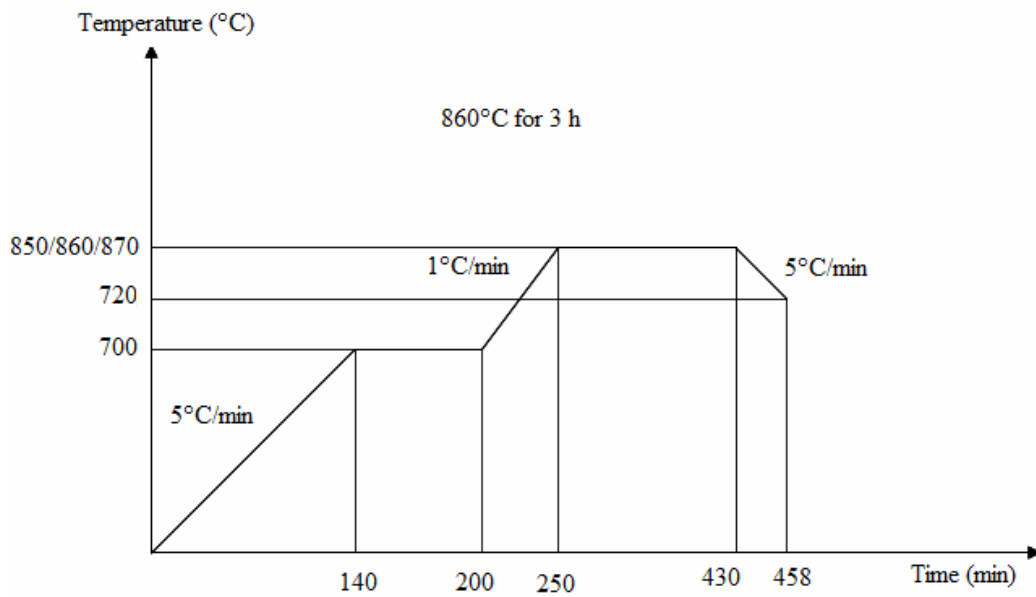
Figure 3. 8: Diagram of the sintering process for the superconducting thin film fabrication

Figure 3. 9: PROTHERM (Model PTF 12/75/200) programmable furnace

The films fabricated at different annealing temperature (850 °C, 860 °C and 870 °C) and time (15 min, 1.5 h and 3 h) will be herein after denoted as Bi-1, Bi-2,

Bi-3, Bi-4, Bi-5, Bi-6, Bi-7, Bi-8, and Bi-9, respectively. The preparation method of the films produced is schematically depicted in Figure 3.10.
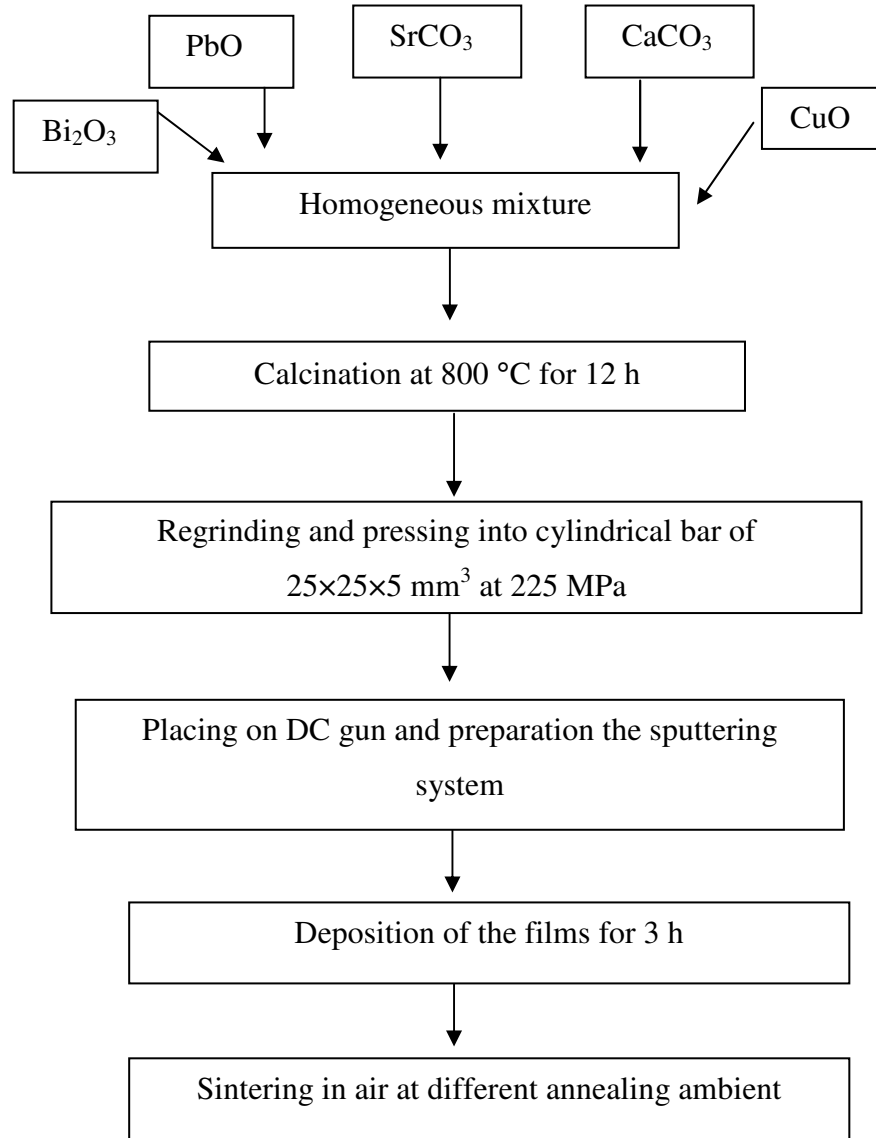
Figure 3. 10: The preparation method of the thin films fabricated in this work

3.5 Characterization of the films

Scanning electron microscopy (SEM), electron dispersive X-Ray (EDX), X-Ray diffraction analysis, resistivity and transport critical current density measurements are performed to determine the effect of annealing ambient on the

microstructural and superconducting properties of the superconducting thin films produced.

3.5.1 Scanning electron microscopy measurements

Scanning electron microscope (SEM) pictures the surface of a material with the aid of a high-energy beam of electrons in a raster scan pattern. After the interaction between the incident electrons and atoms in the material, a signal containing the information about the surface topography, texturing and composition of the material appears. In this thesis, crystallinity, grain size and grain connectivity of the samples studied are examined by means of Scanning Electron Microscopy (SEM) JEOL 6390-LV (Figure 3.11), operated at 20 kV. The SEM micrographs of the fractured surfaces are pictured in the secondary electron image mode at X5000 magnification.

Figure 3. 11: JEOL JSM-6390LV Scanning Electron Microscope

3.5.2 Electron dispersive X-Ray measurements

Energy-dispersive X-Ray (EDX) is a useful method to perform the elemental analysis or chemical characterization of a material. As well known at rest, an atom has ground state (or unexcited) electrons in discrete energy levels. The incident beam (high-energy beam of charged particles) can excite an electron in an inner shell of an atom and in fact ejecting the electron from the shell. Hence, a hole appears in the inner shell. Accordingly, an electron from an outer (higher-energy) shell fills the hole appeared. The energy between the outer and the inner shell can be released in the form of a photon. Energy-dispersive spectrometer can be used to measure the number and energy of the photon emitted from the material. By analyzing the photon emitted, the elemental composition of the material studied can also be determined. In this dissertation, the elemental compositions and distributions in the samples studied are examined with the help of an Oxford X-ray micro-probe analysis connected to SEM (EDX). IXRF SYSTEMS Model 550i Analyzer (Figure 3.12) is used to investigate the photon (x-rays) emitted from the films.

Figure 3. 12: IXRF Systems Model 550i Analyzer

3.5.3 X-Ray Diffractometer measurements

X-Ray diffractometer is one of the most important instruments to examine the structure of a material from the scattering pattern. The working mechanism depends on the interaction between high-energy beams of radiation or charged particles and a material. In this work, the phase compositions of the samples are characterized by XRD investigation with the aid of a Rigaku MultiFlex 2kW diffractometer (Figure 3.13) with Cu Kα radiation (λ=1.5418 Å) in the range 2θ=3–60° at a scan speed of 3°/min and a step increment of 0.02° at room temperature. The measurements are carried out under beam acceleration conditions of 38 kV/28 mA. Phase purity and lattice parameters are estimated from the XRD patterns. The accuracy in determining the lattice parameters (*a* and *c*) is found to be ±0.0001 Å. Additionally, the average sizes of the crystal of the samples are inferred from the Scherrer–Warren approach [118, 119] as a result of the broadening nature in the XRD peaks.

Figure 3. 13: Rigaku MultiFlex 2kW X-Ray Diffractometer

3.5.4 Resistivity measurements

The electrical properties of the samples prepared in this work are examined by dc resistance versus temperature measurements using 1 mA dc current through the samples in the temperature range from 20 to 130 K sample in the He gas contact cryocooler from CRYO Industries (Fig. 3.14).

Figure 3. 14: Cryostat system for the resistivity measurements

Both voltage and current contacts are made with silver paint to minimize the contact resistance. A Keithley 220 programmable current source and a Keithley 2182A nano-voltmeter (Fig. 3.15) are used for the standard four-probe measurements, which allow us to find the true specimen resistance without consisting of the contact resistance between the probes and the specimen [120, 121]. With the aid of the current and voltage measured, the resistivity of the thin film studied is determined by the following relations;

$$R = \frac{\rho L}{A} \text{ and } V = I.R \tag{6}$$

$$\rho = \frac{RA}{L} = \left(\frac{V}{I}\right)\left(\frac{A}{L}\right)$$ (7)

where ρ denotes the resistivity of a material, L is the distance between the inner electrical contacts, and A presents the cross-section of the film.
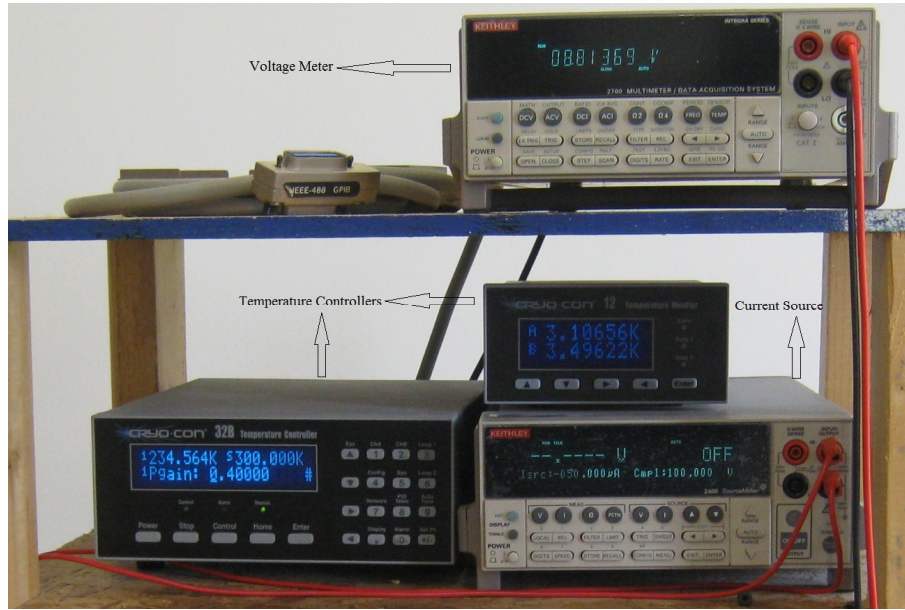
Figure 3. 15: Keithley 220 programmable current source and Keithley 2182A nano-voltmeter

Additionally, a temperature value, where the resistance started to decrease significantly, is determined to be the onset critical temperature (T_c^{onset}) of the samples whereas the offset transition temperature (T_c^{offset}) is defined as the temperature at which $R = 0\Omega$ (within the sensitivity of the measurement system).

3.5.5 Critical current density measurements

The measurement of the potential difference between the inner contacts is used to obtain the maximum current passing through a material or critical current density of a material when the current applied to the material is regularly enhanced at the constant temperature where this material exhibits the superconducting properties

41

and so the potential difference is recorded as zero. However, when the critical value is reached, the potential difference starts to increase immediately due to the presence of the resistance. In this work, transport critical current of the samples in self-field is measured by the same system at 4.2 K in zero field using the conventional four-probe method. A programmable temperature controller (Lakeshore 340) is used for the accurate monitoring of the temperature with a stability and accuracy of ±0.01 K. The current applied parallel to the direction of the surface is ramped at a constant rate (10mA/s) for the entire sample. The critical current (I_c) values of the samples are defined with the criterion of 1 µV/cm. The J_c values are calculated from the I_c and the total cross-sectional area (width 5 mm× thickness 1 µm) of the samples studied. All the data obtained are recorded using the Labview computer software.

3.5.6 Atomic force microscopy measurements

Morphological features (thickness, grain size, average roughness and rms roughness) of the superconducting thin film prepared annealed at 860 °C for 3 h are investigated with the aid of atomic force microscopy, AFM, (Nanomagnetic Instrument, Figure 3.16) based on the forces experienced by a probe as it approaches a surface to within a few angstroms. A typical probe has a radius of 500 Å and is mounted on a cantilever obtaining a spring constant less than that of the atom-atom bonding. The spring is deflected to be within 0.1 Å by the attractive van der Waals (and other) forces and repulsed as it comes into contact with the surface. The surface morphology of a material studied can be plotted with the help of the deflection constant and its position due to the no current flow. The AFM image can be taken for electrically conductive or non- conductive surfaces and in air, vacuum, or fluid environment. Moreover, the AFM can be operated in three modes: (I) contact, (II)

noncontact and (III) tapping. In this study, the topographic and phase images are taken in the non-contact mode under room conditions with typical rate of about 1 line per second with a resonance frequency of about 300 kHz. Measurements are performed with 512 scan lines. Several regions on the specimen surface are scanned to observe the similar images.

Figure 3. 16: Atomic force microscopy, AFM, (Nanomagnetic Instrument)

AFM images analysis is done with special software written by Nanomagnetic Instrument group. Analysis is carried out in the non-contact mode. Moreover, the AFM measurements are conducted with an imaging aspect ratio of 1 : 4 to minimize the signal distortion in the scan slow direction due to thermal drift [122–125]. Height asymmetries (surface skewness and kurtosis) for the film are also discussed clearly.

3.5.7 Magnetoresistivity measurements

After the determination of the optimum sintering ambient for the Bi-2223 superconductor film fabrication, the resistivity measurements as a function of the

magnetic field direction (dc magnetic field and the angle between the surface of the film and the applied magnetic field) in the applied magnetic field up to 3 T are conducted by the standard four-probe technique from 130 K down to 20 K on the superconducting thin film annealed at 860°C for 3 h at constant driving current of 1 mA. The magnetic fields generated from the superconducting coil magnet (CRYO Industries) are applied at different angles (0° to 90° by 15° steps) to the direction of the driving current. Measurement data automated using GPIB interfaced by a personal computer are recorded with the aid of the Labview computer software. Moreover, onset (T_c^{onset}) and offset (T_c^{offset}) critical temperatures, irreversibility field ($\mu_0 H_{irr}$) and upper critical field ($\mu_0 H_{c2}$) of the samples are deduced from the magnetoresistivity curves. The temperature-dependent resistance at constant applied magnetic field is R($\mu_0 H_{irr}$, T)= 0.1 R_n for the $\mu_0 H_{irr}$(T) and R($\mu_0 H_{c2}$, T)=0.9 R_n for the $\mu_0 H_{c2}$(T), respectively. R_n is the normal state resistance of the samples at 95 K [126–129]. The intercepts of extrapolation of $\mu_0 H_{irr}$(T) and $\mu_0 H_{c2}$(T) to zero on the temperature axis are taken as the direct $\mu_0 H_{irr}$(0) and $\mu_0 H_{c2}$(0), respectively [130]. The determined upper critical magnetic field and irreversibility field at the absolute zero temperature predict us to find coherence length (ξ) and penetration depth (λ) values, respectively. Further, activation energy values are determined via the thermally activated flux creep (TAFC) model calculating the pinning energy by making linear fits to the low resistivity part of the transition [131–133]. Moreover, we measured the transport critical current density (J_c) as a function of dc magnetic field and the angle (ϕ), between the surface of the film and the magnetic field on the Bi-2223 film. According to the results obtained, the weak links between the superconducting grains, anisotropic nature, and the pinning ability of the film produced are also discussed in detail.

CHAPTER 4

4. RESULTS AND DISCUSSIONS

4.1 Electrical resistivity measurements

In order to investigate the effect of annealing ambient on the superconducting properties of the samples studied in this work, dc electrical resistivity as a function of temperature is measured in the temperature range from 20 to 130 K and the results obtained are depicted in Figure 4.1.
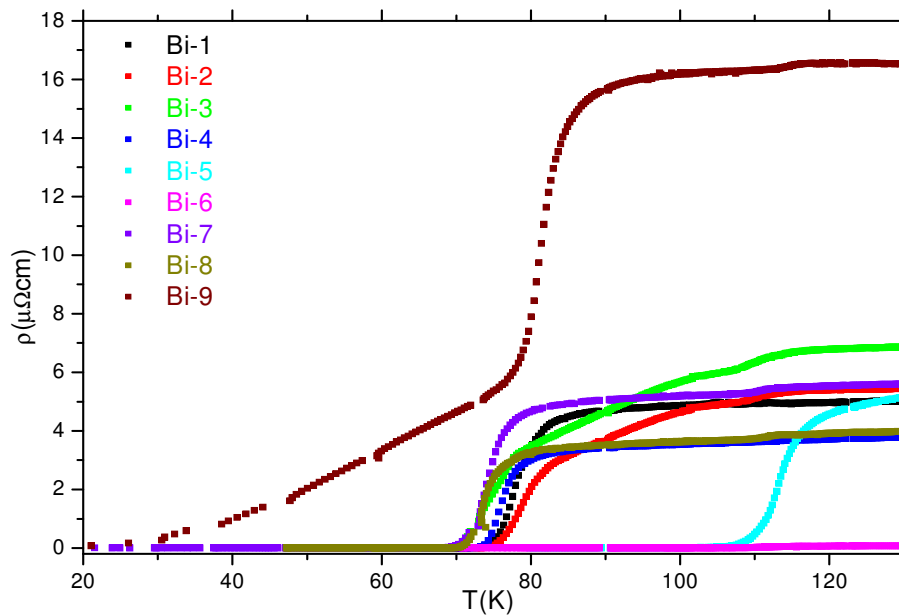
Figure 4. 1: Resistivity as a function of temperature curves for the samples

It is clearly visible that all the samples show metallic behaviour above the T_c (T_c^{offset}) value and the Bi-6 sample is less resistive than the other samples. The room

45

temperature (at 300 K) resistivity of the samples are listed in Table 4.1.

Samples	T_c^{onset} (K)	T_c^{offset} (K)	ΔT_c (K)	Resistivity at 300K ($\mu\Omega cm$)	Hole Concentration P
Bi-1	84.6	73.5	11.1	53.8	0.11953
Bi-2	111.2	74.5	36.7	58.3	0.12133
Bi-3	112.1	69.4	42.7	63.2	0.11226
Bi-4	79.6	72.7	6.9	43.4	0.11814
Bi-5	109.6	92.9	16.7	100.1	0.12265
Bi-6	117.6	102.1	15.5	1.2	0.13033
Bi-7	76.5	69.4	7.1	133.9	0.11286
Bi-8	78.3	72.8	5.5	46.7	0.11831
Bi-9	85.1	22.8	62.3	168.6	0.06588

Table 4. 1: Resistivity measurement results for the samples

As seen from the table that the resistivity is found to be about 1.2 mΩ cm (minimum) for Bi-6 and 168.6 mΩ cm (maximum) for Bi-8 sample, respectively. The resistivity values of the films annealed at 850 °C are found to be close to each other. Moreover, the onset critical (T_c^{onset}) and offset critical (T_c^{offset}) temperatures deduced from the normalized resistance graphs (Figure 4.2.) are given in Figure 4.3.
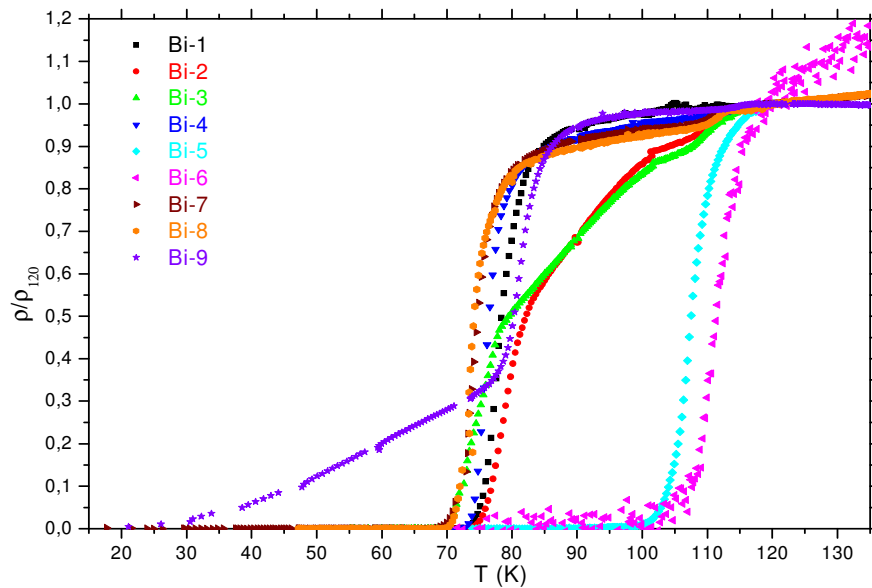
Figure 4. 2: Normalized resistivity versus temperature graphs

The critical transition temperatures (T_c^{offset}) of the films studied in this work are observed to be in a range of 23-102 K. The Bi-6 obtained the maximum T_c value of 102 K; on the other hand, the minimum T_c is noted to be about 23 K for the Bi-9 film.
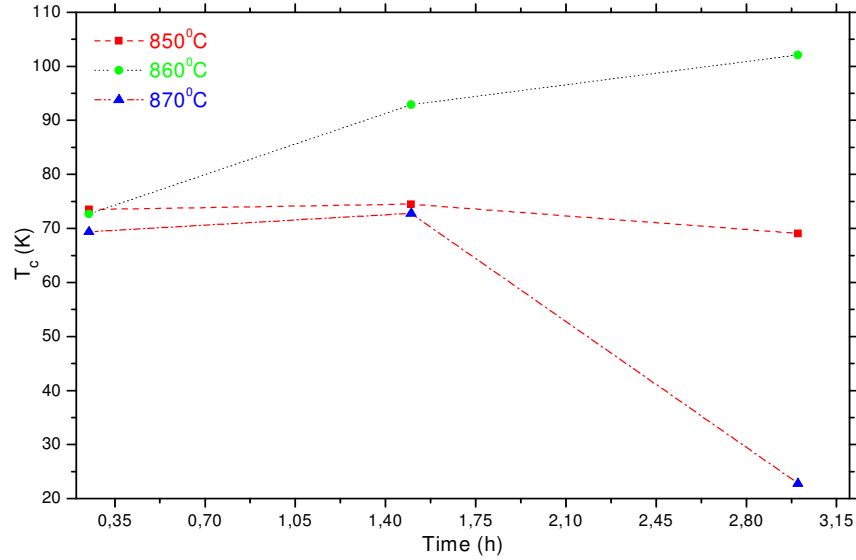
Figure 4. 3: Variation of T_c of the samples with different annealing temperature (The dash line is the guide for eyes)

Moreover, the T_c values of the films prepared at 850 °C did not change considerably with the increase of the annealing time while that of the samples annealed at 870 °C degraded with the increase in the time (see Figure 4.3). In addition, the variations of ΔT_c (T_c^{onset}-T_c^{offset}) are illustrated in Table 4.1, indicating that the annealing time and temperature affected dramatically on the broadening of the resistive transition of the samples. It is visible from the table the minimum ΔT_c is observed to be about 5.5 K for the Bi-8 film while the maximum ΔT_c is obtained to be about 63 K for the Bi-9 sample. This phenomenon can be explained by the presence of impurities and weak links between the superconducting grains and grain misorientations [134], which will be supported by the SEM measurements. Based on

the results,

❖ The critical transition temperatures of the films annealed at 850 °C are found
to be close to each other.

❖ The T_c values of the samples sintered at 860 °C are noticed to be changeable
and the T_c is observed to enhance with the increase in the annealing time.

❖ The T_c is found to decrease with the increase of the time for the samples
produced at 870 °C.

❖ The maximum variation between the T_c^{onset} and T_c^{offset} values is noted to be 60
K for the sample annealed at 870 °C for 3 h.

❖ The minimum ΔT_c (5.5 K) is observed for the film annealed at 870 °C for 1.5
h.

❖ For the Bi-2223 thin film fabrication, the optimum ambient is determined to
be 860 °C (for the annealing temperature) and 3h (for the annealing time),
respectively.

4.2 XRD analyses

Figure 4.4a-b indicates the X–ray diffraction patterns between 3° and 60° for
the thin films annealed in different conditions. The (Bi, Pb)-2223 peaks are presented
by H (*h k l*) Miller indices while the peaks of (Bi, Pb)-2212 phase are shown by L (*h
k l*) Miller indices given in the diagrams. All the samples studied in this work
exhibited the polycrystalline superconducting phase. It is observed form the figure
that the Bi-6 sample illustrated the highest peak intensities belonging to Bi-2223
phase while the Bi-2212 phase is found to be denser than other phase in the Bi-9
sample. In other words, not only are (*0 0 l*) peaks dominant features in the Bi-6 film,
but also the Bi-2223 phase is more dominant than the Bi-2212 phase. Based on the

results, the optimum annealing ambient is determined to be 860 °C for 3h to obtain the formation of (Bi, Pb)-2223 phase, favored by the results of the resistivity measurements.
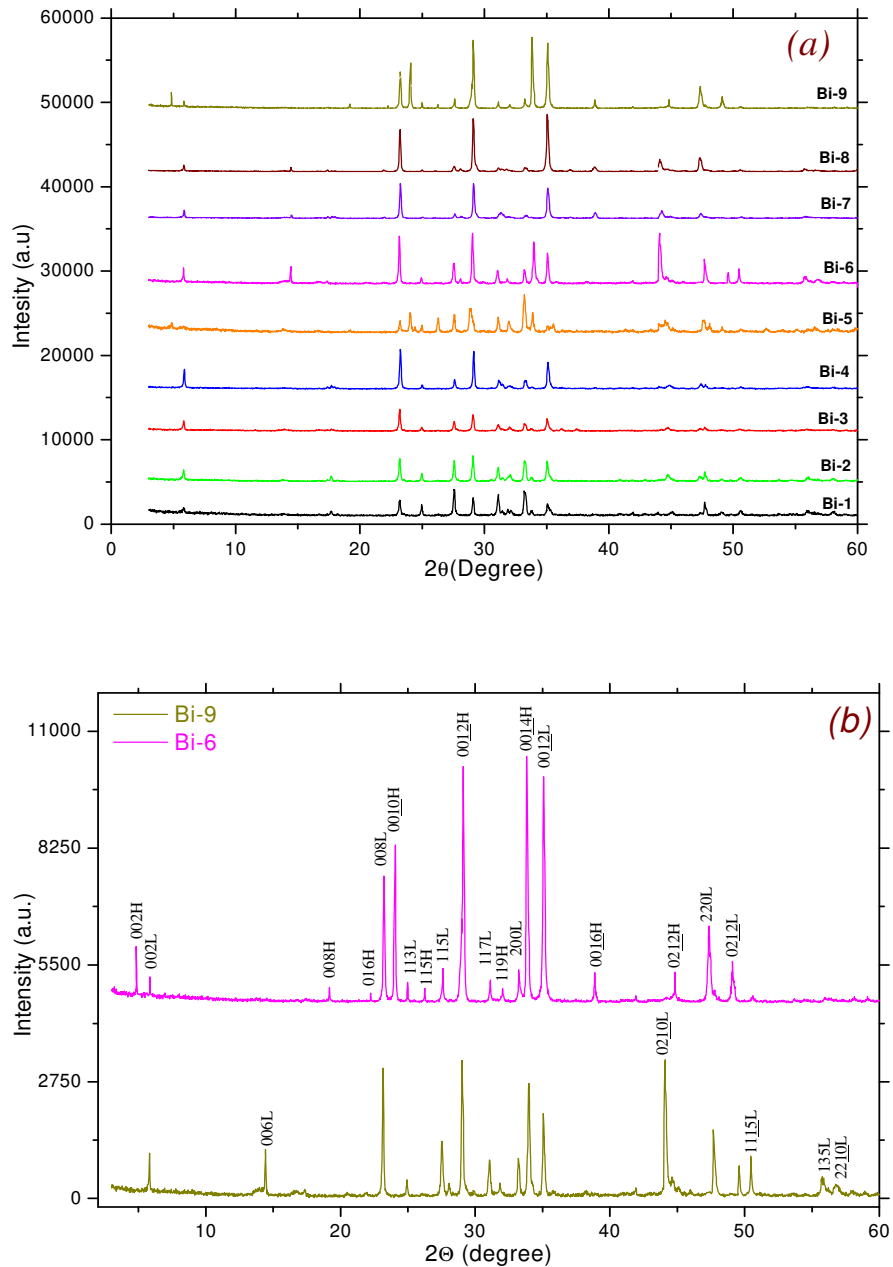
Figure 4. 4: (a): XRD patterns of all the samples prepared and (b): XRD patterns of the Bi-6 and Bi-9 with miller indices

The relative percentages of (Bi, Pb)-2223 and (Bi, Pb)-2212 phases computed by using the following relations (8) and (9) are tabulated in Table 4.2.

$$f_{(2223)} = \frac{\sum I_{H(hkl)}}{\sum I_{H(hkl)} + \sum I_{L(hkl)}} \quad \text{and} \quad f_{(2212)} = \frac{\sum I_{L(hkl)}}{\sum I_{H(hkl)} + \sum I_{L(hkl)}} \qquad \text{(8) and (9)}$$

where I gives the peak intensity of the present phase.

Moreover, the lattice parameters a and c are calculated using the least square method through d value and $(h\ k\ l)$ planes for tetragonal unit cell structure. Their variations as a function of the annealing time are also depicted in Table 4.2.

Samples	a (Å)	c (Å)	Volume fraction (%)		J_c (A.cm^{-2})	Grain size (nm)
			2223	- 2212		
Bi-1	5.42	32.53	40.23	59.77	844.54	482
Bi-2	5.43	30.67	46.36	53.64	59.42	386
Bi-3	5.35	35.45	52.42	47.58	548.13	440
Bi-4	5.61	30.54	5.89	94.11	1283.96	486
Bi-5	5.37	37.02	84.37	15.63	631.98	475
Bi-6	5.42	37.16	88.65	11.35	2068.09	509
Bi-7	5.44	30.41	44.91	55.09	302.51	425
Bi-8	5.38	30.72	47.78	52.28	395.39	468
Bi-9	5.74	30.84	38.43	62.57	20.42	342

Table 4. 2: XRD measurement results for the films prepared in this work

As seen from the table, the lattice constant, a, of all the samples prepared is found to be close to each other while the largest lattice constant, c, is obtained for the Bi-6 sample. In addition, Figure 4.4b depicts the XRD graphs of Bi-6 and Bi-9 sample. As seen from the figure, some peak intensities such as *(0012)H*, *(016)H*, and *(119)H* decreased dramatically whereas the other peak intensities including *(002)H*, *(008)H*, *(016)H*, *(0010)H*, *(115)H*, *(0014)H*, *(0016)H* and *(0212)H* disappeared

50

completely. However, *(006)L, (02<u>10</u>)L, (115)L, (135)L and (22<u>10</u>)L* peaks started to appear entirely. Based on the results, the annealing ambient of Bi-6 is determined to be optimum to obtain the Bi-2223 phase. These findings are also ascertained by both the resistivity and SEM measurements. Besides, the broadening nature of the XRD peaks provides that the particle sizes of the samples are found to be within the nanometer scale [135–139] by using the Scherrer–Warren equation. According to the equation, in broadening region the average size of a crystal is defined as;

$$d = 0.941\lambda / B\cos\theta_B \tag{10}$$

where d denotes the thickness of the crystal, λ is the wavelength, B presents the fullwidth half maximum (FWHM) of the Bragg peak corrected using the corresponding peak in micron-sized powder and θ_B is the Bragg angle. Moreover,

$$B^2 = B_m^2 - B_s^2 \tag{11}$$

where B_s is the halfwidth of the standard material in radians. The calculations indicate that the largest grain size is obtained for the Bi-6 sample (Table 4.2).

4.3 Hole-carrier concentration calculation

The hole-carrier concentrations per Cu ion, P, are calculated by means of the following relation [140]:

$$P = 0.16 - \left[\left(1 - \frac{T_c}{T_c^{\max}}\right)/82.6\right]^{1/2} \tag{12}$$

where $T_c^{\max}$ is taken as 85 K for Bi-2212 phase [141] and 110 K for (Bi, Pb)-2223 phase [142] and T_c values are deduced form Figure 4.3.
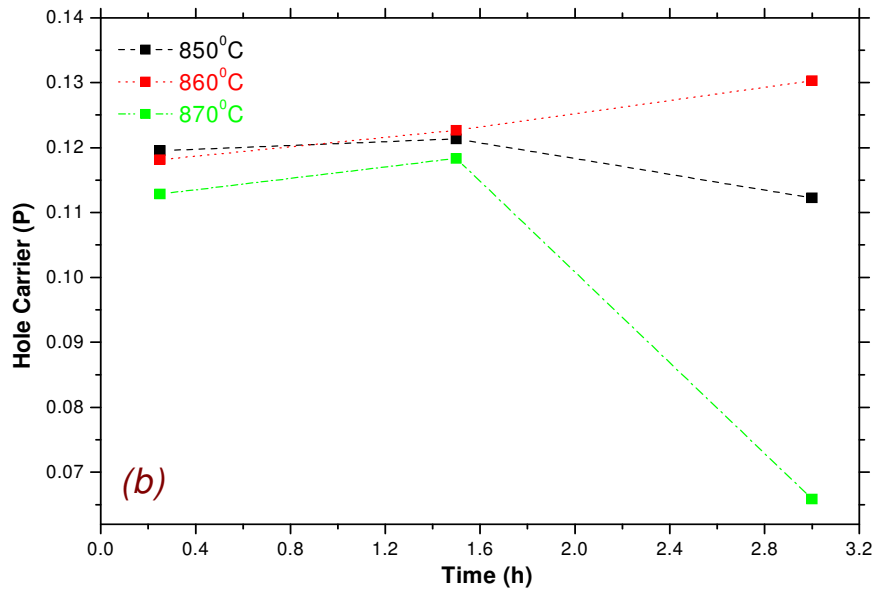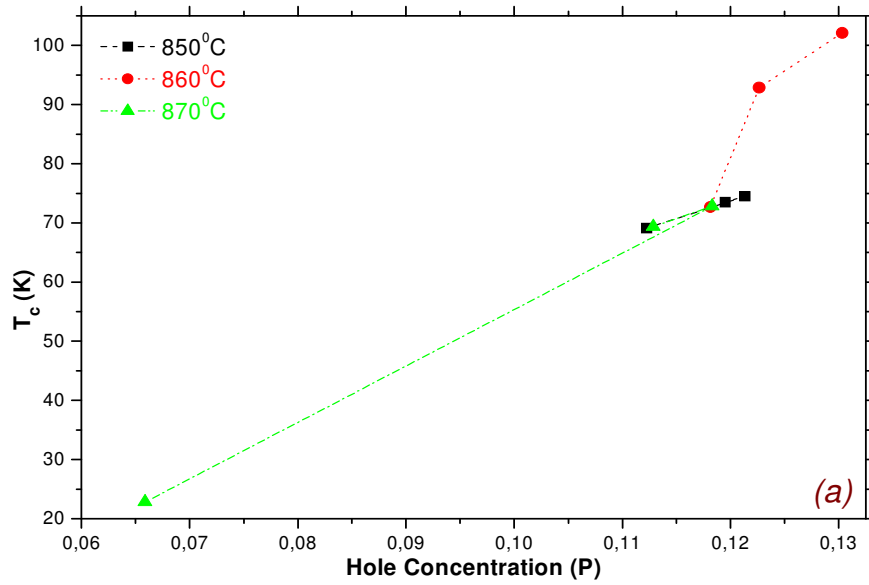
Figure 4. 5: (a): Variation of critical temperature versus hole-carrier concentrations and (b): Variation of hole-carrier concentrations versus time for the samples (The dash line is the guide for eyes)

Fig. 4.5a illustrates the linear-like relationship between the superconducting transition temperature and hole-carrier concentrations, confirming the effect of the carrier concentrations on the superconducting materials. Fig. 4.5b also depicts the change of P as a function of the annealing time and temperature. The hole-carrier

concentration of the Bi-6 sample obtaining the highest critical temperature is observed to be greater than the others (Table 4.1).

4.4 SEM analyses

The surface morphology images of the samples produced are performed by Scanning Electron Microscopy (SEM). Figure 4.6a-i indicates the SEM images of the fractured surface of all the films. As seen from the figure, the granular morphology of some samples consists primly from flaky layers of large platelet-like structure with random alignment distribution, which reveals the layered growth mechanism, typical of (Bi, Pb)-2223 phase formation [143–146].
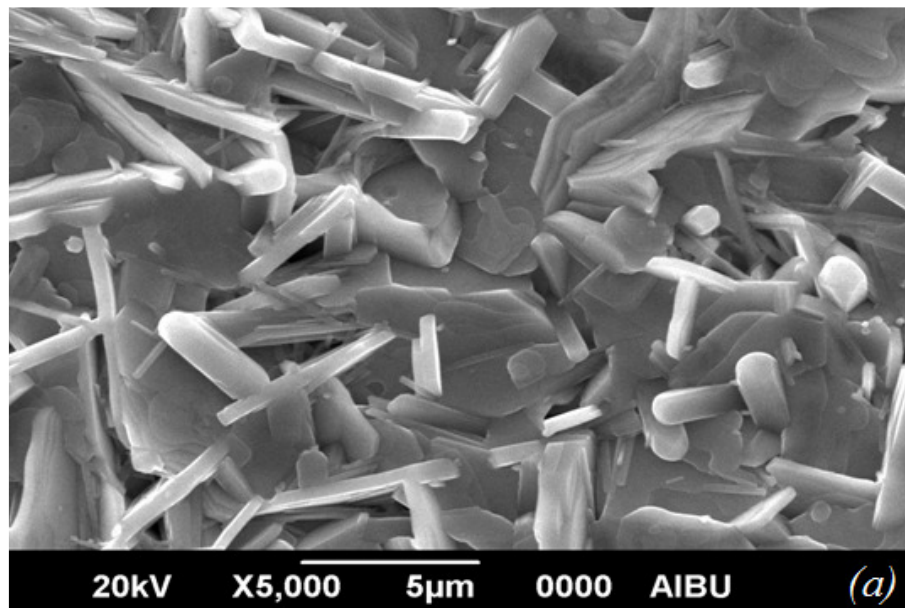
Figure 4. 6: SEM micrographs of (a) Bi-1 sample (Continued)
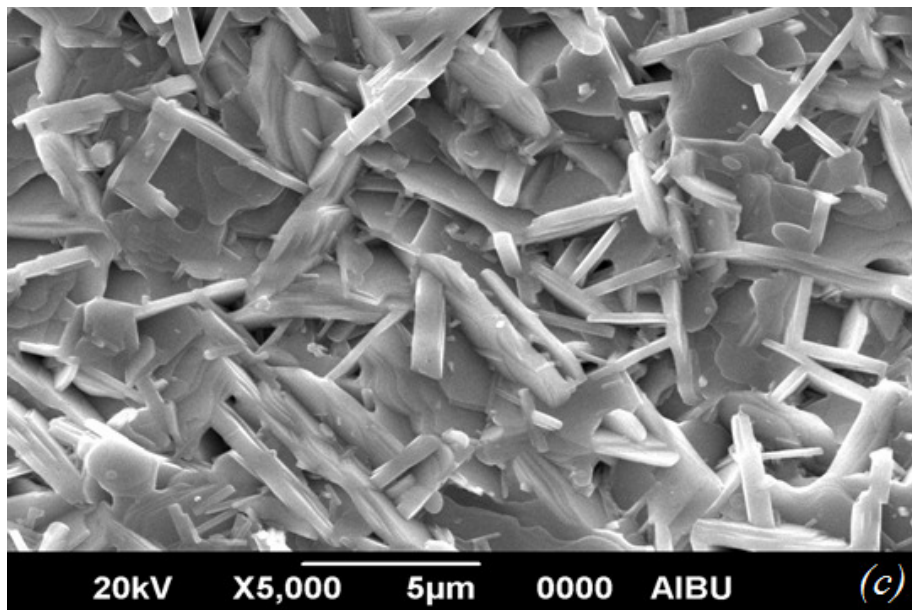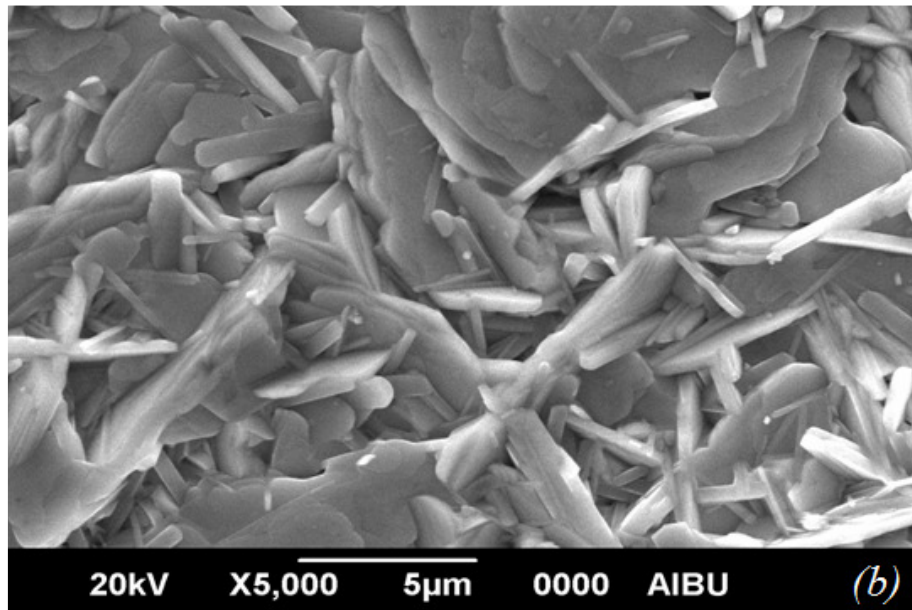
Figure 4. 6: (b) Bi-2 and (c) Bi-3 samples (Continued)
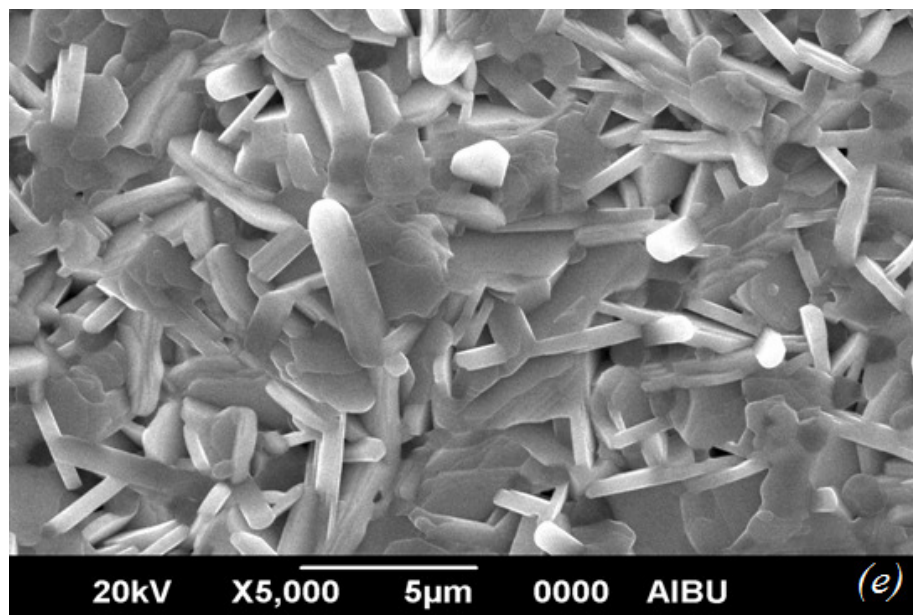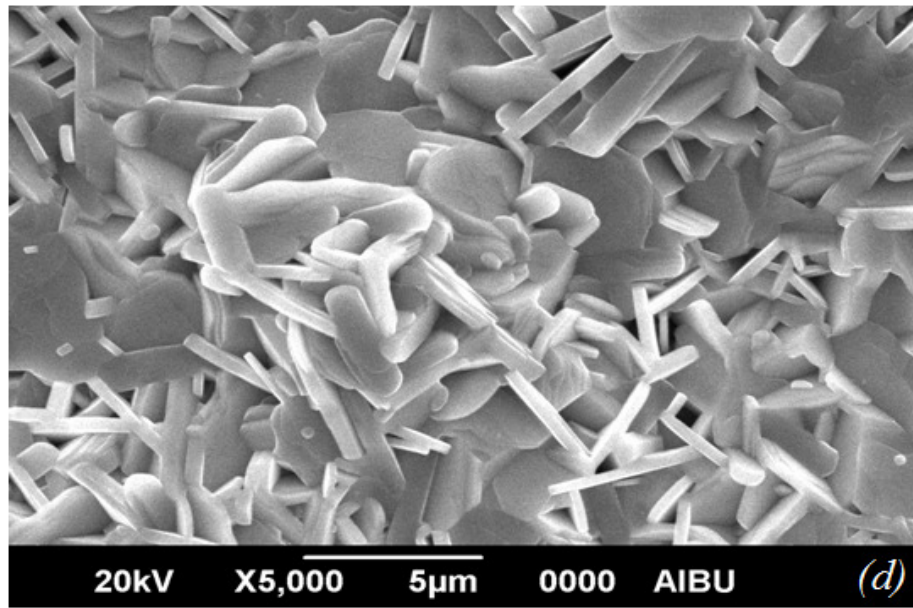
Figure 4. 6: (d) Bi-4 and (e) Bi-5 samples (Continued)
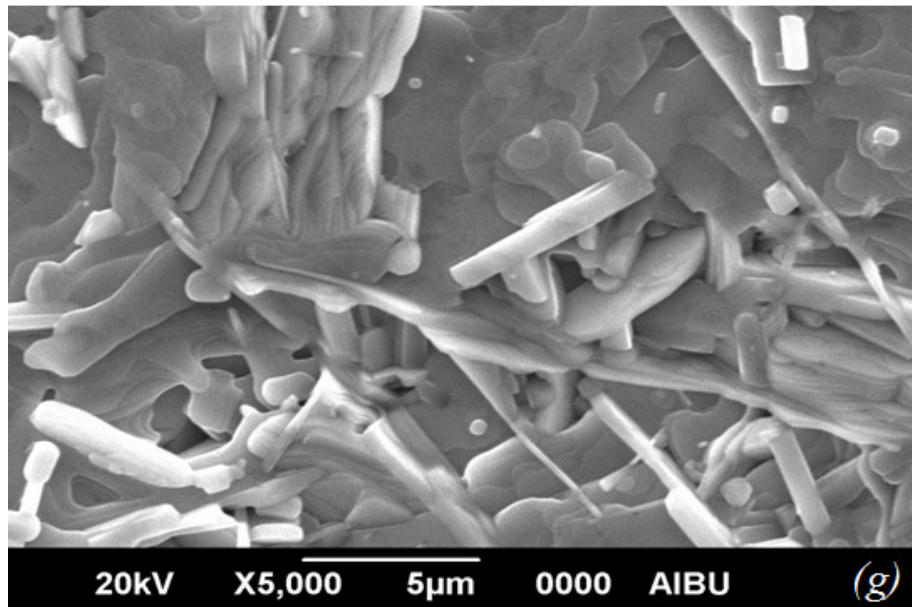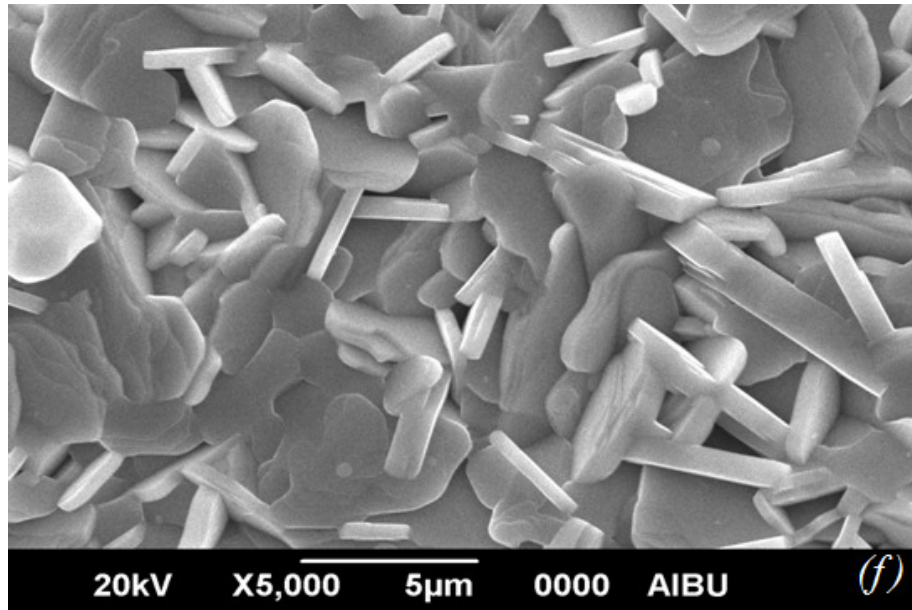
Figure 4. 6: (f) Bi-6 and (g) Bi-7 samples (Continued)
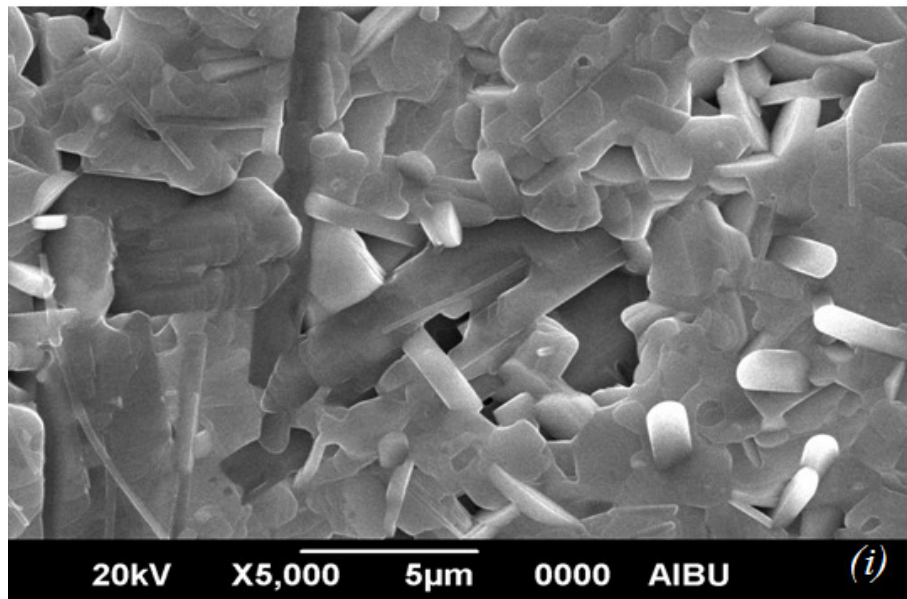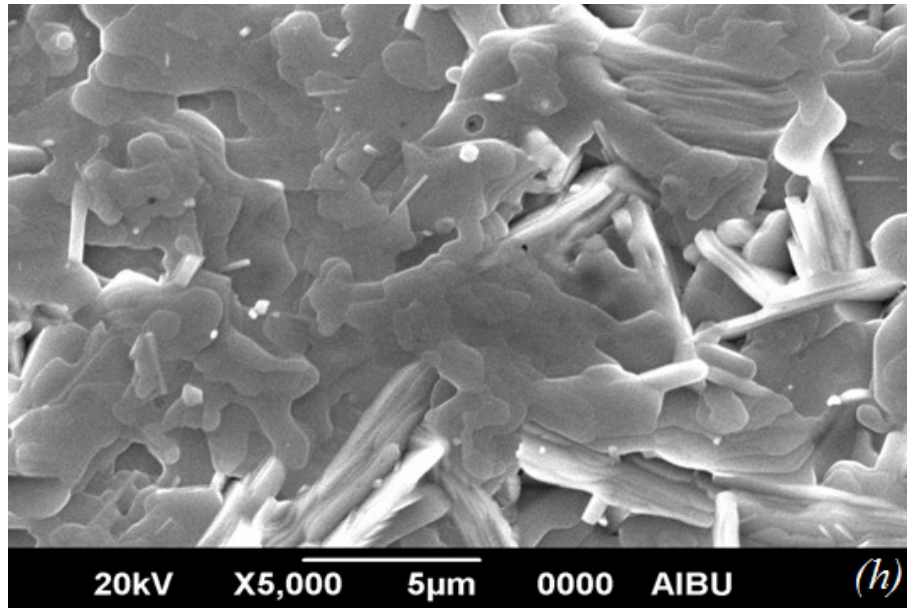
Figure 4. 6: (h) Bi-8 and (i) Bi-9 samples prepared for this dissertation

However, with the change of the annealing time and temperature, the platelet grains linked well in the samples can be degraded due to the random orientation, weak links between the grains, the increase in the partial melting, level of impurities, voids, and porosity associated with formation of a smaller plat-like grains (the basic

characteristics of (Bi, Pb)-2212 phase formation) [147]. It is visible that SEM photograph of the Bi-6 sample obtaining leafy appearance [148–151] presents a broad grain size distribution and the best crystallinity in comparison with the others (Fig 4.6.f). Additionally, the surface of the sample is more uniform with better alignment of grains. On the other hand, the Bi-9 sample has the worst appearance among these samples and there are voids and signs of partial melting on the micrograph of the sample. Although it is not possible to determine the grain sizes exactly, according to the image processing, the average grain sizes are obtained to be about 520 and 350 nm for the Bi-6 and Bi-9 samples, respectively. According to the results of the SEM measurements, the Bi-6 sample has the largest average crystallite size, the best surface morphology and grain connectivity. In conclusion, we examine that how the annealing ambient affects the structural properties of the films studied.

4.5 EDX analyses

The elemental composition analyses of the samples are analytically investigated with the aid of the electron dispersive X-ray (EDX). Figure 4.7 presents Bi, Sr, Ca, Cu and O element composition mappings taken on the surface of all the samples produced in this work. As can be seen from the figure, the elements used for the preparation of samples are observed to distribute homogeneously (Figure 4.7), revealing that all the elements are observed to incorporate into the crystalline structure of the samples studied.
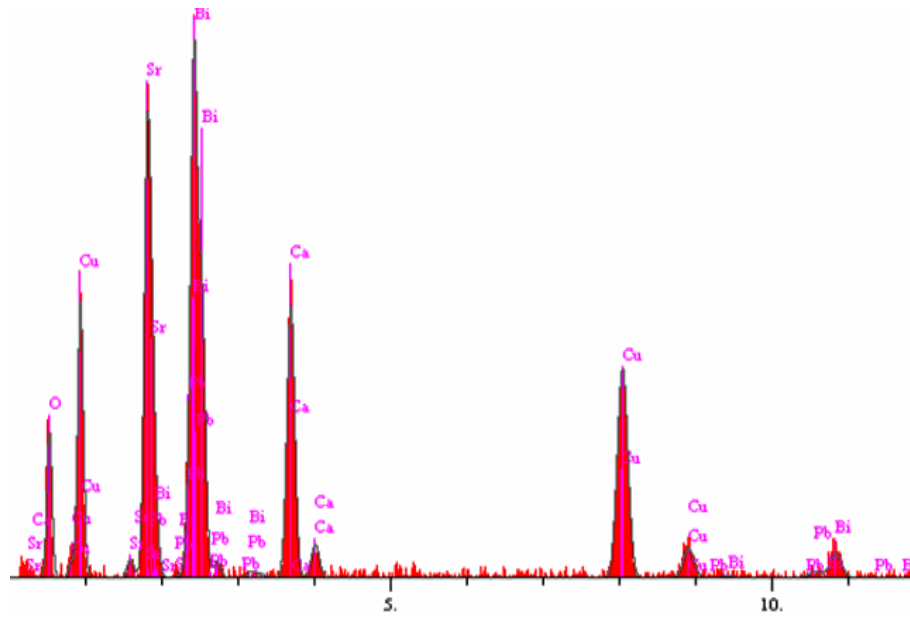
Figure 4. 7: EDX image of distribution of the elements in the samples

However, Pb and Cu elements of the Bi-6 sample are found to be more than that of the other samples (Table 4.3), which confirms the superconducting properties of the sample might be more superior to the other ones.

Element	Line	Concentration (wt.%)								
		Bi-1	**Bi-2**	**Bi-3**	**Bi-4**	**Bi-5**	**Bi-6**	**Bi-7**	**Bi-8**	**Bi-9**
O	K_α	18.4	17.4	16.6	17.0	18.7	17.8	18.9	17.5	18.6
Ca	K_α	7.21	7.4	8.2	7.9	7.5	7.33	7.9	7.3	7.3
Cu	K_α	16.8	15.1	16.8	15.3	15.1	18.5	15.3	18.5	17.7
Sr	L_α	24.1	24.4	23.1	24.1	22.9	21.5	22.2	22.7	22.5
Pb	L_α	5.4	4.8	6.8	6.6	5.7	7.0	6.3	6.69	3.6
Bi	L_α	28.1	30.9	28.7	29.2	30.1	27.8	29.4	27.5	30.0

Table 4. 3: Concentrations of the elements in the samples produced

Besides, the oxygen element in the samples studied is observed to be variable and the maximum oxygen content is obtained for the Bi-3 sample. Hence, it is concluded that the superconducting properties such as T_c and J_c do not depend strongly on the oxygen content in the system.

4.6 Transport critical current density

There are several methods [152–155] to explain the pinning mechanism in a thin film. One of them is to measure the critical current density (J_c). Figure 4.8a shows the role of the annealing ambient on the self field critical current density of the thin films prepared in the present work. As seen from the figure, J_c values of the films are found to be in a range of 59-2068 A/cm^2 at 4.2 K (in liquid hydrogen). Here, while the smallest J_c is observed for the Bi-9 sample, the maximum J_c is obtained for the Bi-6 sample.

Moreover, there is a sharply decrease in the J_c of the films annealed at 850 and 860 °C for 1.5 h whereas that of the film annealed 870 °C for 1.5 h slightly increases. This dramatic change in J_c values is attributed to the increase of the increased weak links between the superconducting grains, porosity, secondary phases, grain boundaries resistance and de-orientation of (Bi,Pb)-2223 grains. Fig. 4.8b also illustrates the critical current density versus critical translation temperature. One can see from the figure, the films produced at 860 °C obtain higher critical temperature and critical current density than others. It is concluded that the highest annealing temperature and time (870 °C for 3 h) studied in this work degrades the superconducting properties of the thin film while the optimum annealing ambient is noted to be 860 °C for 3h for the formation of (Bi, Pb)-2223 phase, supporting the results of the structural observations. An improvement of the J_c value is associated

with not only the reduction of the porosity and weak links between the superconducting grains but also the increase in the flux pinning centers, the average length of the cell parameter c, the grain size and their orientations [156]. Thus, the film annealed at 860 °C for 3 h has the greatest superconducting properties.

In other words, the critical current density in the crystals can be improved by introducing the effective flux pinning centers. As well known, when a magnetic field applies to a type-II superconductor it penetrates into the material in the form of vortices. Each vortex carries a flux quantum $\Phi = h/2e$, and consists of both a cylindrical core of a radius ξ (called as coherence length) and a current circulating around the core out to a distance λ (named as penetration depth of the material) [157]. Therefore, the current flowing into the superconductor material generates the energy dissipation as a result of the Lorentz force, leading to the mobility of vortices and the disappearance of superconductivity in the material.
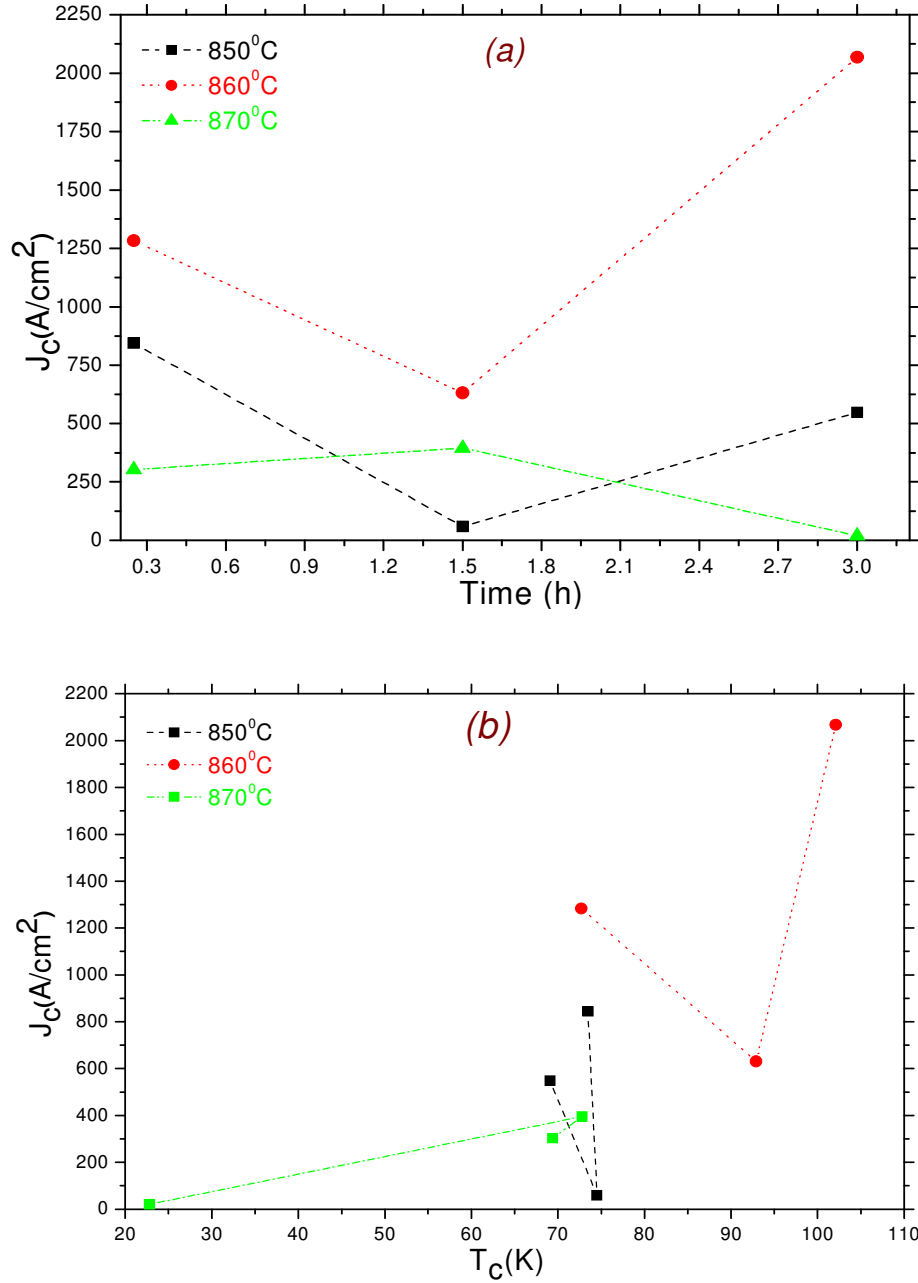
Figure 4. 8: (a): J_c versus annealing time graph and (b): J_c versus critical temperature graph (The dash line is the guide for eyes)

Nevertheless, the vortices mobility can be minimized by introducing defects which pin these vortices. Hence, the J_c value of a material is in accordance with the flux pinning of vortices. Besides, an effective flux pinning centers in a material can easily be produced by means of the defects such as stacking faults, pores/voids, screw dislocations, twin boundaries, planar and micro-defects [158, 159]. Here, the

annealing ambient of 860 °C for 3 h enhancing the J_c value might lead to appear the effective flux pinning centers (defects) in the sample studied.

4.7 Magnetoresistivity analyses

After the determination of the optimum annealing ambient, the variation of resistivity as a function of the magnetic field direction (dc magnetic field and the angle between the surface of the film and the applied magnetic field) for the superconducting thin film prepared at 860 °C for 3 h using the DC magnetron reactive sputtering technique at 100 watt under various applied magnetic field ranging from 0 to 3 T is measured in the temperature range of 20–130 K. Figure 4.9 and Figure 4.10 display the normalized resistivity versus temperature plots under field strengths of 0, 0.01, 0.03, 0.1, 1, 2 and 3 T, which are parallel and perpendicular to the film surface, respectively. Whereas the T_c of the film without magnetic field is found to be about 102 K, it is noted to decrease to 90 K for the field applied parallel ($\mu_0 H \perp c$-axis) and 83 K for the field applied perpendicular ($\mu_0 H // c$-axis) to the surface of the film for 0.01 T (Table 4.4).
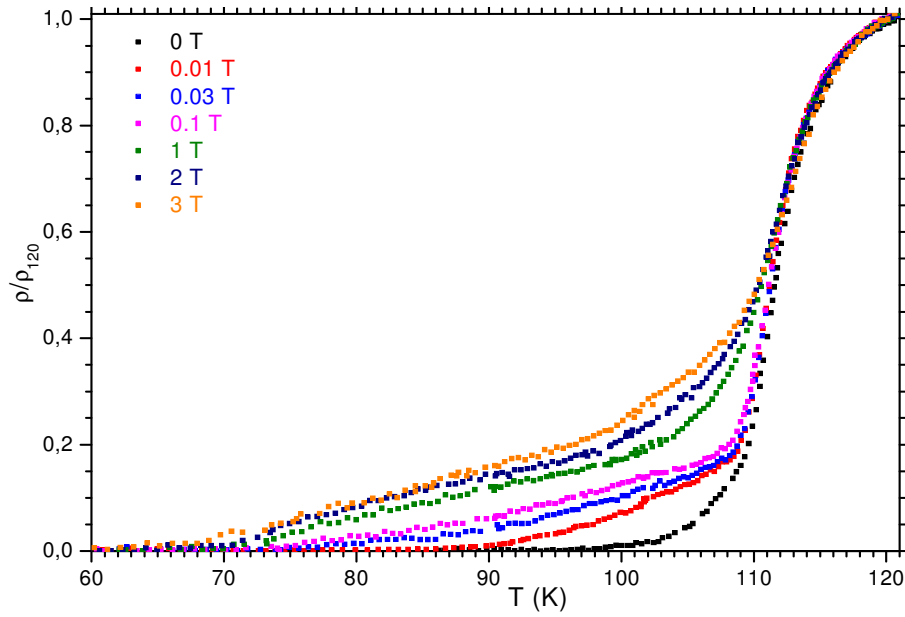
Figure 4. 9: Resistivity versus temperature graph under various magnetic field parallel to the film surface
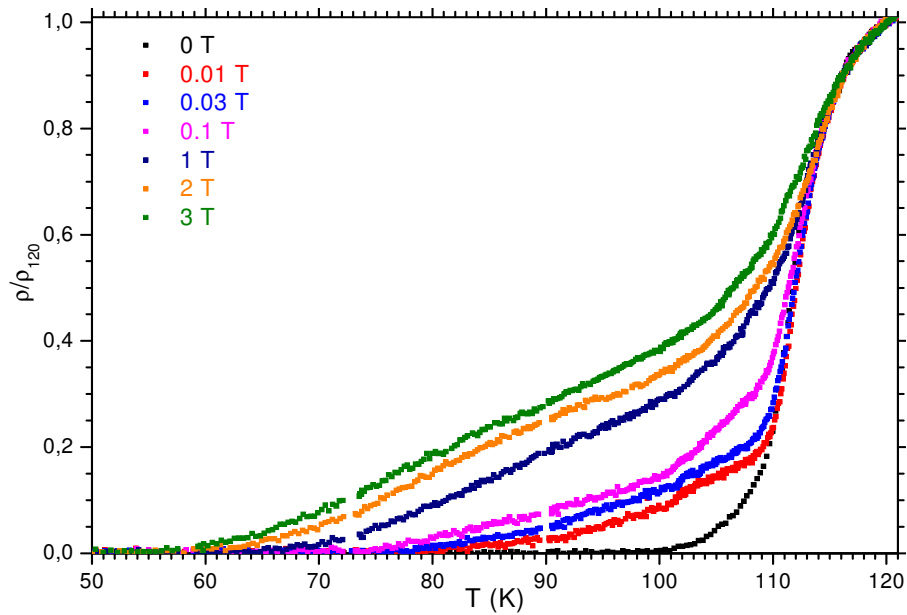
Figure 4. 10: Resistivity versus temperature graph under various magnetic field strength perpendicular to the film surface

The decrease in T_c is very prominent for higher external fields, for example, the T_c decreases to 60 K (69 K) for $\mu_0H//c$-axis ($\mu_0H\perp c$-axis) at 3 T. Resistivity versus temperature measurements are carried out for the field-surface angles of ϕ=0, 15, 30, 45, 60, 75 and 90°.

Critical Temperatures (T_c^{offset})				
Applied Fields	$\phi=0°$	$\phi=30°$	$\phi=60°$	$\phi=90°$
0 T	102 K	102 K	102 K	102 K
0.01 T	90 K	86 K	84 K	83 K
0.03 T	80 K	78 K	77 K	76 K
0.1 T	78 K	74 K	74 K	70 K
1 T	75 K	70 K	69 K	66 K
2 T	72 K	68 K	65 K	63 K
3 T	69 K	65 K	63 K	60 K

Table 4. 4: Zero resistivity transition temperatures (T_c) of the Bi-2223 thin film under various applied magnetic fields and angles

In this work, the discussion of the resistivity results for $\phi=0$ and 90° is enough to understand the anisotropic nature of the film produced. There are two main observations on the field dependence of the resistivity versus temperature. The transition temperature and width increase with the enhancement of the external field and the effect is more prominent for the field parallel to the c-axis of the film. The latter observation might indicate that flux flow phenomenon is more dominant in $\mu_0H//c$-axis compared to $\mu_0H\perp c$-axis [160].

4.8 Irreversibility and upper critical field

The temperature dependence of the irreversibility fields and upper critical fields calculated for all angles is presented in Figure 4.11a-b. As seen from the figure the μ_0H_{irr} and μ_0H_{c2} curves of the sample prepared are observed to shift to lower temperatures as the amount of angle increased.
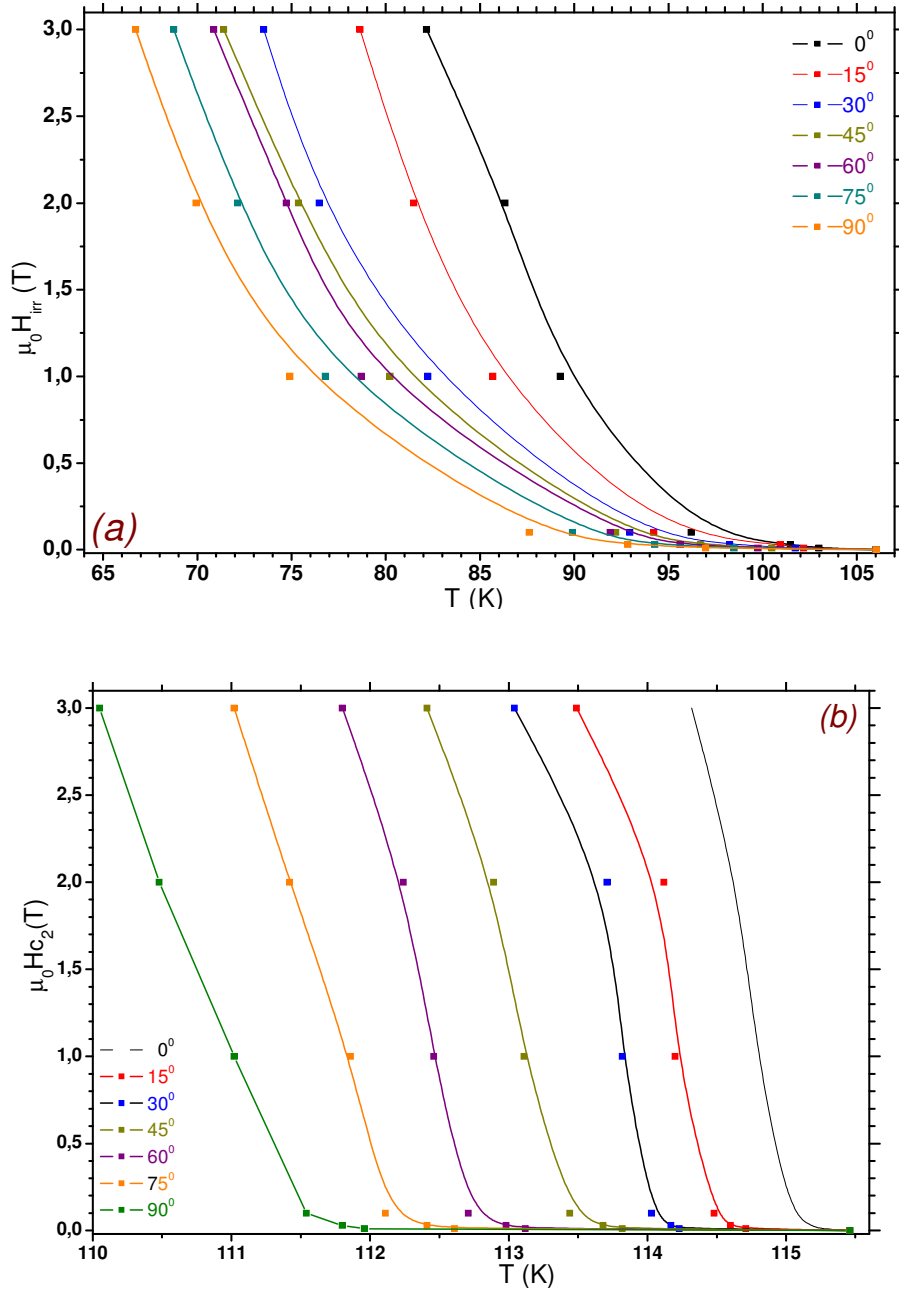
Figure 4. 11: (a): μ_0H_{irr} and (b): μ_0H_{c2} versus temperature plots for different field angles

Moreover, these calculated values are noted to increase with descending the temperature. The extrapolations of the curves at T=0 K are also used to calculate the $\mu_0H_{irr}(0)$ and $\mu_0H_{c2}(0)$ values of the sample [130, 161]. The $\mu_0H_{irr}(0)$ values are observed to decrease from 12.37 T at ϕ=0° to 6.98 T at ϕ=90°. Likewise, the $\mu_0H_{c2}(0)$ values are obtained to decrease from 332.97 T at ϕ=0° to 51.94 T at ϕ=90°

(Table 4.5). It is clearly seen from the figure, the position of the irreversibility line at $\phi=0°$ is higher than the others. The increase of the angle between external magnetic field and c-axis decreases the position of the irreversibility lines, which shows the pinning ability of the sample also decreases with increasing angle. The change of the irreversibility as a function of the angle indicates the anisotropy of the fabricated film. In addition, at absolute zero temperature coherence length and penetration depth are often calculated from upper critical magnetic field and irreversibility field respectively, because of the fact that these parameters are difficult quantities to measure directly. The coherence length $\xi(0)$ and penetration depth $\lambda(0)$ at T=0 K are computed using $\xi(T)=[\phi_0/2\pi\mu_0 H_{c2}(T)]^{1/2}$ and $\lambda(T)=[\phi_0/2\pi\mu_0 H_{irr}(T)]^{1/2}$, where $\phi_0=2,07\times10^{-15}$ Weber (Tm^2).

Degree (°)	$\mu_0 H_{irr}(0)$	$\mu_0 H_{c2}(0)$	Coherence Length (Å)	Penetration Depth (Å)
0	12.37	332.97	9.94	51.58
15	11.40	193.13	13.05	52.40
30	8.62	143.65	15.14	53.74
45	8.20	103.84	17.80	63.34
60	7.98	74.21	21.06	64.23
75	7.44	61.83	23.07	66.53
90	6.98	51.94	25.17	68.69

Table 4. 5: Irreversibility fields, upper critical fields, penetration depths and coherence lengths of the Bi-2223 superconducting thin film at absolute zero temperature

The values obtained are also tabulated in Table 4.5. As can be seen from the table, the coherence lengths are calculated to be 9.94, 13.05, 15.14, 17.80, 21.06,

23.07 and 25.17 Å; on the other hand the penetration depths are also computed to be 51.57, 52.40, 53.74, 63.34, 64.29, 66.53 and 68.69 Å for the field-surface angles of ϕ=0, 15, 30, 45, 60, 75 and 90°, respectively.

4.9 Activation (pinning) energy

Activation energy plays an important role as a potential energy barrier to keep the magnetic flux in pinning center. The activation energy as a function of the applied magnetic field at different angles in the range from 0° to 90° can be calculated by means of the results of the resistive transitions under the applied magnetic fields. The resistive transition measurements in various applied magnetic fields are useful tool to determine the magnetic field dependence of the effective activation energy. For temperatures below the T_c value, the thermally assisted flux creep (TAFC) is an important dissipation mechanism causing a long resistive tail [162–166]. In this study, in order to get more accurate values of activation energy, we performed the transport measurements instead of magnetic measurements due to the widening of the magnetic translation. Firstly, the activation energies are calculated using line pinning model and making linear fits to the low resistivity part of the transition [162, 167]. Secondly, $\ln\rho$ versus 1/T curves are plotted and activation energy values of the sample at various angles are determined from the slopes of the linear part of the low resistivity region.
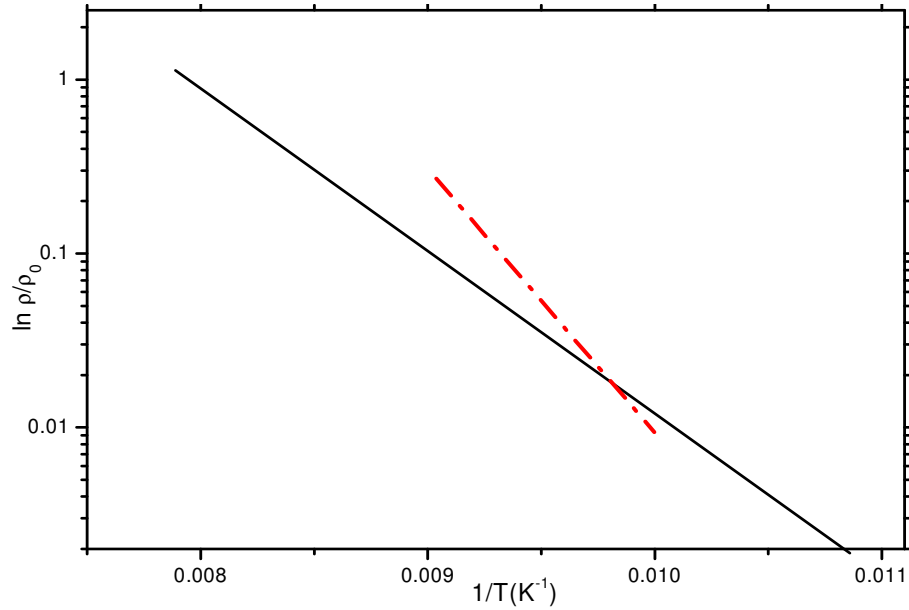
Figure 4. 12: The linear fit of the $\ln\rho/\rho_0$ versus 1/T plots graph for the Bi-2223 thin film without any magnetic field at $\phi=0°$. The line is guides to the eye

In Figure 4.12, linear fit of the Arrhenius plot of the $\ln\rho/\rho_0$ versus 1/T graph for the sample is presented. The graphs, which are given in Figure 4.13, show $\ln\rho/\rho_0$ versus 1/T plots of the sample in the applied magnetic field at different angles.

The result deduced from the semi logarithmic Arrhenius plots of Figure 4.13 shows that there is an exponential dependence of ρ with 1/T. According to the result obtained, the energy dissipation stems from the thermal activation of flux across the pinning barrier. The resistivity, ρ, can be evaluated from Arrhenius law $\rho=\rho_0 \exp(-U_0/k_BT)$ [168–172]. The activation energies of the sample studied are determined from the slope of the straight lines and also depicted in Table 4.6.
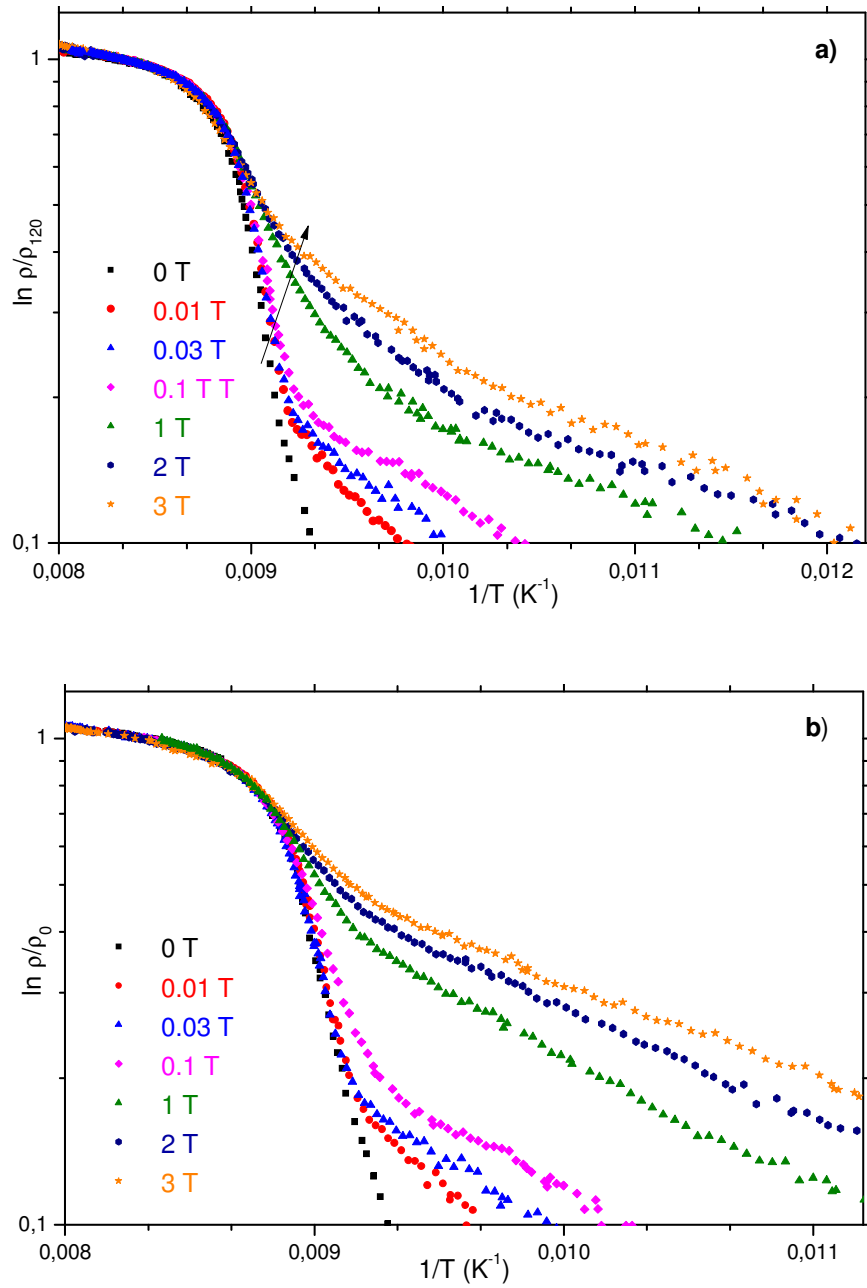
Figure 4. 13: ln resistivity versus 1/T graphs of the Bi-2223 thin film: a) $\phi=0°$ correspond to $\mu_0 H \perp c$-axis and b) $\phi=30$ (Continued)
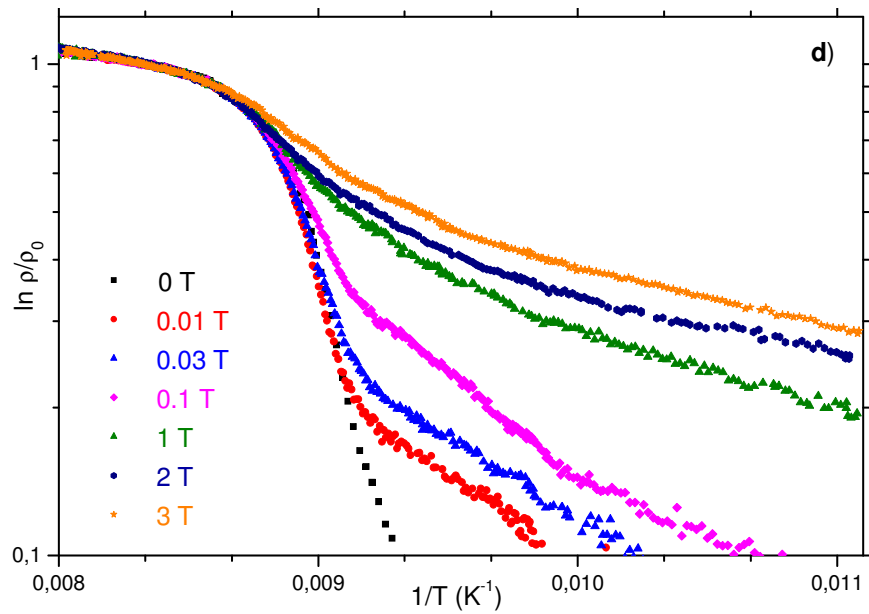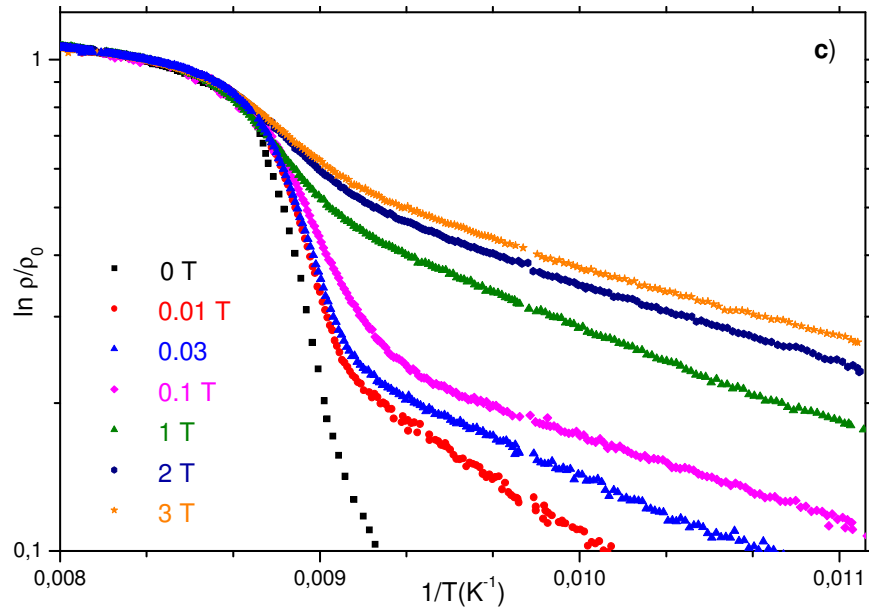
Figure 4. 13: c) ϕ=60°, and d) ϕ= 90° correspond to $\mu_0 H // c$-axis. The slopes of the linear parts of the low resistivity region are used to calculate the activation energy

As seen from the table, the activation energy calculated to be about 2405 K at zero magnetic field ($\mu_0 H$=0) is found to tend to decrease with increasing the applied magnetic fields. While there is a slightly change in the activation energy up to angle of 60°, the energy change is noted to decrease sharply at angle of 75° and 90°.

	Activation Energies (K)						
Angles	0 T	0.01 T	0.03 T	0.1 T	1 T	2 T	3 T
ϕ=0°	2405	2360	1987	1374	702	525	439
ϕ=15°	2405	2321	1902	1312	636	487	376
ϕ=30°	2405	2282	1842	1246	618	459	349
ϕ=45°	2405	2218	1790	1205	544	424	305
ϕ=60°	2405	2195	1764	1189	512	378	298
ϕ=75°	2405	1285	854	492	184	134	104
ϕ=90°	2405	1085	703	386	130	84	64

Table 4. 6: Activation (pinning) energy values as a function of the applied magnetic field at different angles for the Bi-2223 thin film

The field and angle dependence of the activation energy may be consistent with the intergrain weak links, grain misorientations and the strong anisotropic behaviour of the sample. Further, the field dependence is investigated by means of the log–log plot of activation energy versus applied magnetic field (Figure 4.14). The relation is found to be linear as seen in the graph. The field dependence of the activation energy can be described by a power law as:

$$U(H) \; \alpha \; H^{-\alpha} \tag{13}$$
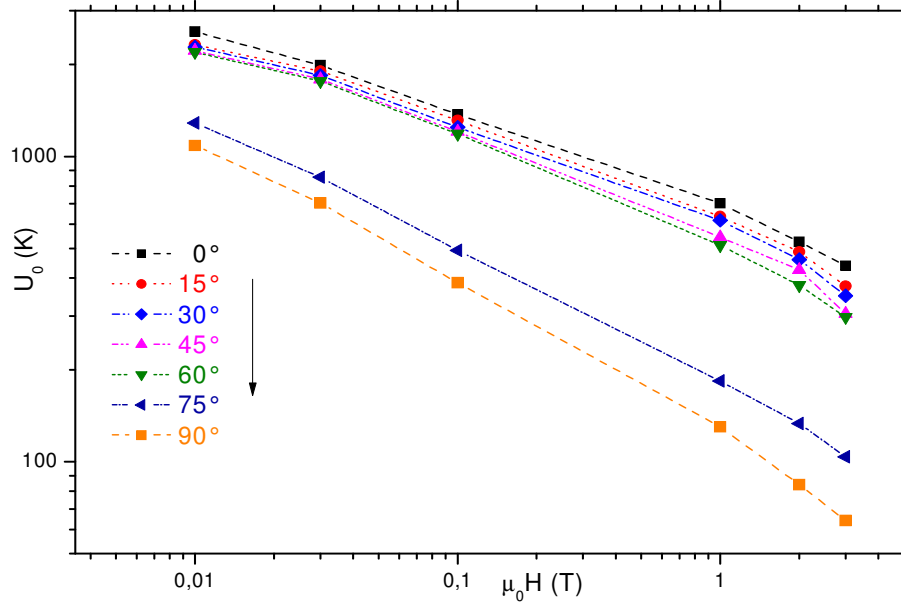
Figure 4. 14: Dependence of activation energy on magnetic field for the Bi-2223 thin film. The lines are guides to the eye

We fitted our data to Eq. (13) and the α value is found to be about 0.498 that is close to 0.5. This means that the activation energy can be associated with the plastic deformation of flux line lattice at dislocations, similar to the thermally activated motion of edge dislocations in crystals [173, 174]. The α value 0.5, is frequently obtained for the BSCCO-2212 system [175–177], the BSCCO-2223 system [178–180] and also for TBCCO thin films [181].

4.10 Transport critical current density as a function of the magnetic field direction

The field dependence critical current density (J_c) measurement is useful method to explain the pinning mechanism in thin film. In this study, critical currents are defined with a criterion of 1 μV/cm electric field. J_c is measured as functions of the applied field and angle between plane and magnetic field direction at 4.2 K by means of a 7 T solenoid-type superconducting magnet. Figure 4.15 shows the field direction dependence of J_c at various magnetic fields such as 0.01, 0.02, 0.04, 0.05,

0.4, 0.8, 1, 1.5, 2, 3, 4, 5, 6, 7 T. The J_c values for all the angles are found to suddenly decrease in the field range between 0 and 1 T while it is determined to remain nearly constant, presenting that the applied magnetic field penetrates only the intergranular media below 0.4 T [182].
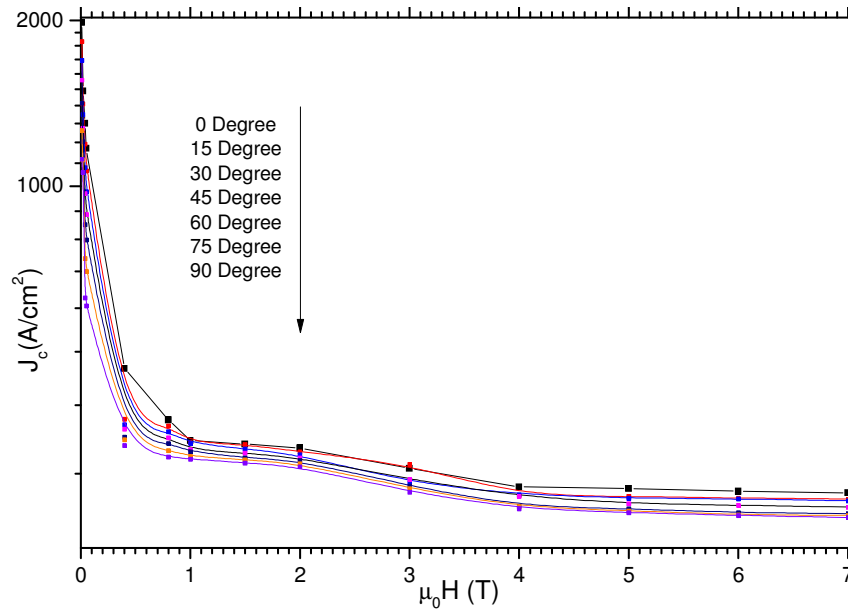
Figure 4. 15: Critical current density versus applied field graph of the film for different angles

$J_c(\phi,\mu_0H)$ graph (Figure 4.16), is also extracted from Figure 4.15 for investigation of pinning mechanism in details. The J_c is found to be 1982, 1833, 1694, 1559, 1417, 1263, 1120 A/cm^2 for $\phi=0$, 15, 30, 45, 60, 75 and 90° at the magnetic field of 10 mT, respectively.
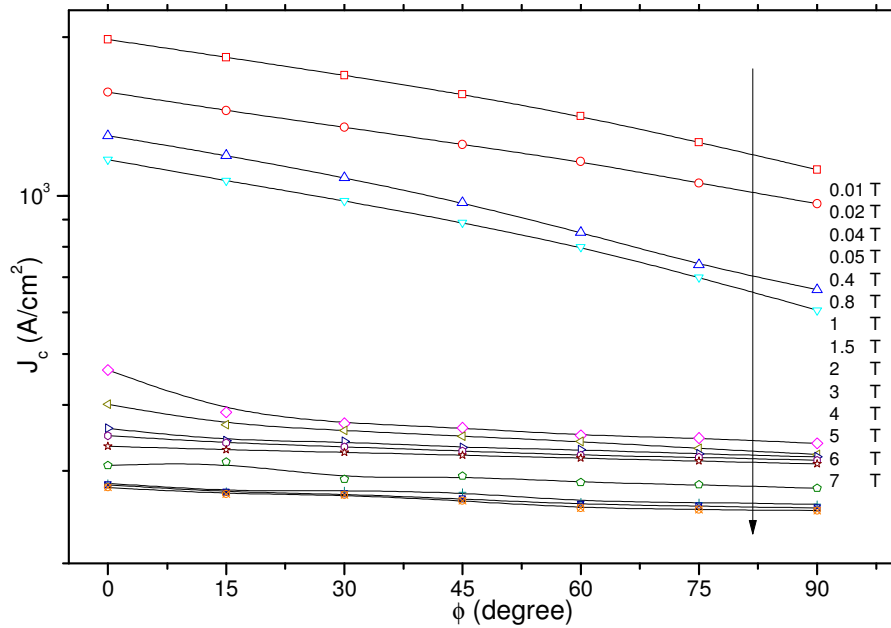
Figure 4. 16: J_c versus ϕ plots at various magnetic fields for the sample studied

The J_c is noted to decrease significantly in the applied magnetic field up to 0.4 T for angle values from 0 to 90°. It is concluded that not only this behavior might be attributed to the flux depinning due to weak pinning, the flux lattice melting and the glass liquid transition [183, 184] but also the anisotropic J_c behavior of the film is due to the intrinsic. Further, decrease in J_c is more rapid with increasing ϕ at 10, 20, 40 and 50 mT while this behavior remains almost constant (plateau region) for above 0.4 T and above 30°. When magnetic field is aligned with defects, any influence of defects on flux pinning can clearly be investigated as J_c anomaly [185].

4.11 Flux pinning forces

Flux pinning force (F_p), which is a strong tool to examine the pinning mechanism of a material, can be calculated by the equation of $F_p = J_c \times B$. The critical current density measurements performed as functions of the applied field and angle (ϕ) between plane and applied magnetic field direction are used to find the pinning

force. Figure 4.17 illustrates the flux pinning force plots at different angles in the range from 15° to 90°. It is apparent from the figure that the maximum pinning force of 17.5 MN/m^3 is observed in the case of applied field parallel to c-axis (μ_0H//c-axis) at the applied magnetic field of 7 T, confirming that the superconducting properties degrade with the increment of both the applied field and angle as a consequence of the anisotropic nature of the Bi-2223 superconducting film.
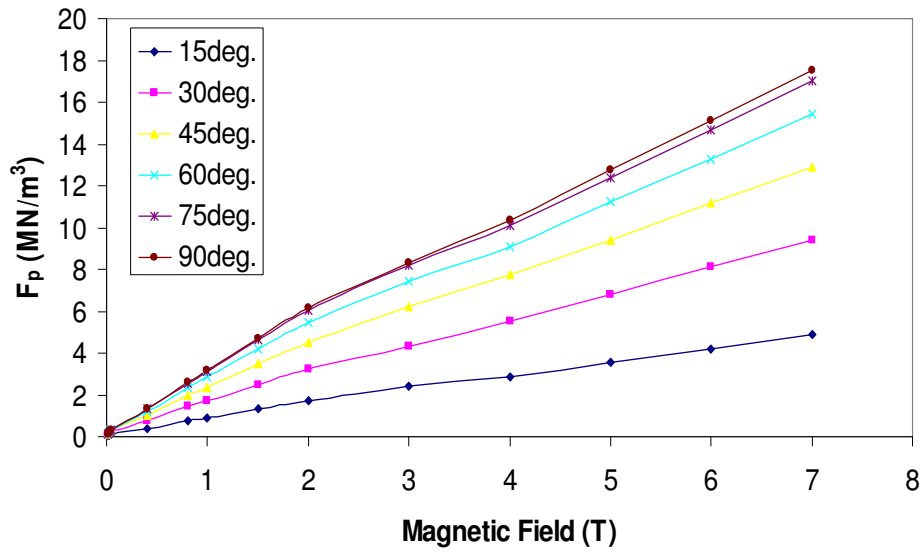
Figure 4. 17: F$_p$ plots of the Bi-2223 thin film at various angles in a range of 15-90°

At the same time, the normalized flux pinning force F_p/F_{pmax} often scales with normalized magnetic flux density $b=B/B_{max}$. Here, F_{pmax} denotes the maximum value of the flux pinning force (F_p) when B_{max} presents the maximum magnetic flux density. The normalized flux pinning force against the reduced magnetic flux density can be analyzed with the aid of the several pinning models [186–189], such as Δ_K pinning $F_p/F_{pmax} = 3b^2(1-2b/3)$, normal point ($\Delta T_c$) pinning $F_p/F_{pmax} = 9/4b(1-b/3)^2$, surface pinning $F_p/F_{pmax} = (25/16)b^{1/2}(1-b/5)^2$ and Kramer equation $F_p/F_{pmax} = b^{1/2}(1-b)^2$. In this thesis, F_p/F_{pmax} versus B/B_{max} curves calculated with regard to the Kramer

equation are plotted in Figure 4.18. One can see from the figure that all the curves obtained exhibit the similar behaviour although the angles are different from each other at the same applied magnetic field. This phenomenon might be explained by the high quality of the superconductor film produced in this work, being favoured by the statistical analysis of the AFM measurements.

4.12 AFM analyzes

Atomic Force Microscopy (AFM) is useful method to both analyze the surface morphology of a thin film and obtain information about the thickness, roughness and height asymmetries values such as the skewness and kurtosis of the film [190, 191]. The average roughness and height asymmetry values obtained are measured using the software analysis written by Nanomagnetic Instrument. The typical AFM image corresponding to the film produced at 860 °C for 3 h is displayed in Figure 4.18. The surface scanned is 32×32 μm. It is visible from Figure 4.18 that the thickness of the film is found to be about 900 nm by means of AFM image.
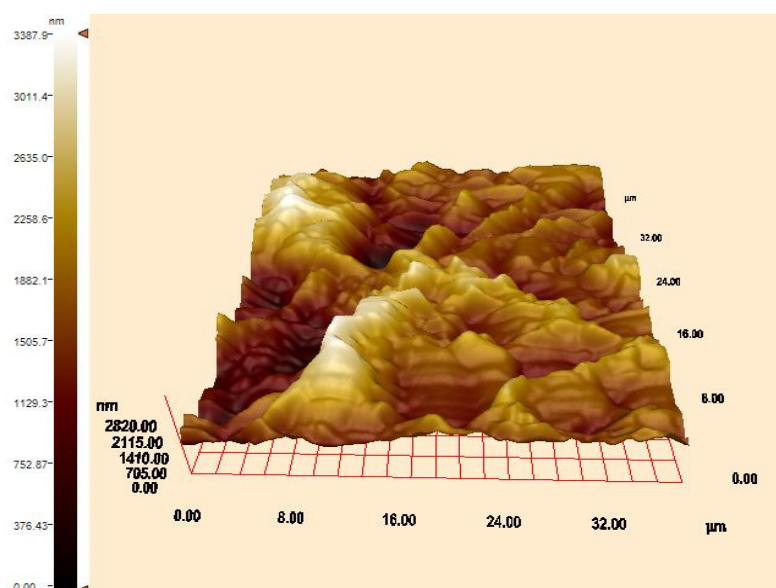
Figure 4. 18: Atomic Force Microscopy image of the DC-sputtered Bi-2223 thin film annealed at 860°C for 3 h

In addition, the average roughness parameter (S_a), the most used surface roughness parameter, is the arithmetic mean or average of the absolute distances of the surface points from the mean plane while rms roughness parameter (S_q) is the root mean square of the surface departures from the mean plane within the sampling area [192, 193]. Average roughness parameter can be calculated using the equation (14),

$$S_a = \frac{1}{MN} \sum_{j=1}^{N} \sum_{i=1}^{M} |z|(x_i, y_j) \tag{14}$$

and rms roughness parameter can be calculated using the equation (15),

$$S_q = \sqrt{\frac{1}{MN} \sum_{j=1}^{N} \sum_{i=1}^{M} z^2(x_i, y_j)} \tag{15}$$

where M denotes the number of columns in the surface and N is the number of rows in the surface. The surface roughness of the sample produced is observed to be highly rough with average roughness 89.7 nm and rms roughness 96.3 nm. Based on the results of the surface roughness, an irregular structure is observed on the surface of the film. This irregular structure, being responsible for the change of the critical temperature and activation energy under the applied magnetic field, represents the strong anisotropic behaviour of the sample clearly. In other words, the difference between average roughness and rms roughness might explain the possible reason for the observed degradation in superconducting properties of the film under the applied magnetic field.

The statistical analysis of AFM image is also performed by using the height distribution histogram as shown in Figure 4.19. The height asymmetry can be

explained by surface skewness and kurtosis from the quantitative surface roughness parameters [194]. Skewness is a measurement for the symmetry of the variation of a surface about its mean plane. A Gaussian surface, having a symmetrical shape for the height distribution, has a skewness of zero.
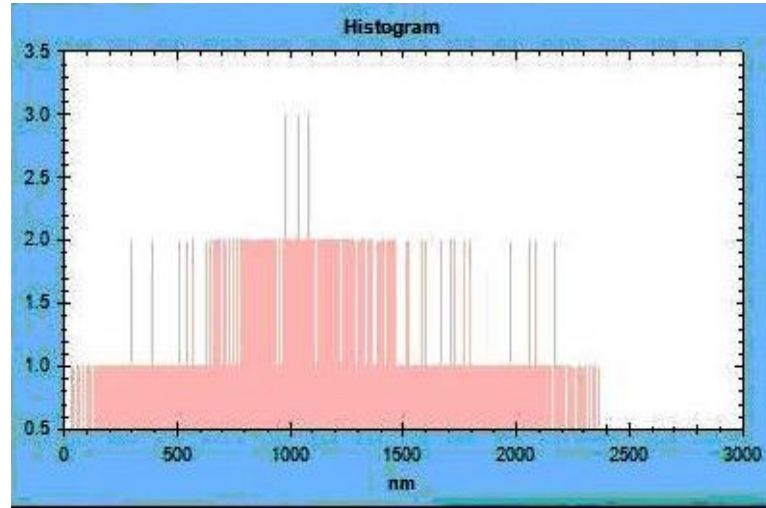
Figure 4. 19: Height distribution histogram of the Bi-2223 thin film

A plateau honed surface with predominant plateau and deep valleys tends to have a negative skew, whereas a surface comprised of disproportionate number of peaks has positive skew. The skewness is calculated using the equation (16).

$$S_{sk} = \frac{1}{MNS_q^3} \sum_{j=1}^{N} \sum_{i=1}^{M} z^3(x_i, y_j) \tag{16}$$

On the other hand, Kurtosis measures the peakedness or sharpness of the surface. A Gaussian surface has kurtosis value of 3. A surface that is centrally distributed has a kurtosis value greater than 3. A surface that has a well spread out distribution has a kurtosis value of less than 3. Kurtosis is calculated using the equation (17).

$$S_{ku} = \frac{1}{MNS_q^4} \sum_{j=1}^{N} \sum_{i=1}^{M} z^4(x_i, y_j) \tag{17}$$

Skewness and kurtosis roughness are also tabulated in Table 4.7. As seen from the table, the skewness is found to be about 1.635 when the kurtosis is obtained to be about 3.107.

Parameters	Bi–2223 thin film
Average roughness	89.7 nm
RMS roughness	96.3 nm
Skewness, S_{sk}	1.635
Kurtosis, S_{ku}	3.107

Table 4. 7: Statistical parameters of the film

Based on the combination of the skewness and kurtosis values, the film surface is found to be centrally distributed and comprised of disproportionate number of peaks. According to interpretation of the surface morphology and statistical parameters, the film produced in this work can be useful for applications in technology and industry. Moreover, for future work we are planning to obtain much smoother surface by changing the production conditions such as annealing ambient, temperature and deposition time so that they might be useful in optical and electronic applications.

CHAPTER 5

5. CONCLUSION

In this dissertation, we fabricated the Bi-based superconducting thin films on MgO (100) substrate using the direct current (DC) magnetron reactive sputtering technique at 100 watt at various annealing temperature (850, 860 and 870 °C) and time (15 min, 1.5 h and 3 h) to obtain the optimum annealing ambient for the Bi-2223 superconducting thin film. The characterization of the films are conducted by means of the scanning electron microscopy, X-Ray diffraction analysis, electron dispersive X-Ray, atomic force microscopy, resistivity and transport critical current density measurements. The results obtained indicate that the optimum annealing ambient is determined to be 860 °C for annealing temperature and 3 h for the annealing time, respectively. Moreover, the magnetotransport measurements as a function of temperature ranging from 15 to 120 K in the applied magnetic field up to 3 T are performed by the zero field cooling (ZFC) procedure to analyze the pinning mechanism and superconducting properties of the Bi-2223 superconductor film. For the superconductivity, some vital data (extracted from the magnetoresistivity curves) such as onset and offset critical temperatures, transition width, activation energy, irreversibility field, upper critical field, penetration depth and coherence length are found and discussed clearly. Finally, the magnetoresistivity and transport critical current density measurements at the different magnetic field direction are executed to investigate the anisotropic behaviour of the Bi-2223 film studied. The flux pinning

energy and force values are obtained by thermally activated flux creep model and Kramer equation, respectively. All the results obtained demonstrate that the electrical, physical, microstructural, pinning mechanism and superconducting properties of the Bi-based superconducting films depend strongly on the annealing ambient and the major conclusions to be obtained from this work are as follows:

- The maximum T_c^{offset} value is obtained to be about 102.1 K for the Bi-6 film whereas the minimum one is found to be about 22.8 K for the Bi-9 sample at zero magnetic field ($\mu_0 H$=0), respectively. Similarly, the highest J_c value of 2068 A/cm^2 is observed for the former sample while the smallest J_c is obtained to be about 59 A/cm^2 for the latter sample.

- SEM images point out that the best texturing, crystallinity and connectivity between grains, largest grain size and lowest porosity are observed for the Bi-6 film. Additionally, EDX investigations show that the elements used for the preparation of samples distribute homogeneously, confirming that all the elements incorporate into the crystalline structure of the samples prepared.

- XRD results signify that all the samples studied exhibit the polycrystalline superconducting phase with the changing intensity of diffraction lines and the greatest Bi-2223 phase fraction and largest cell parameter a and c are obtained for the Bi-6 sample film, leading to not only the enhancement in the T_c^{offset} value but the phase change from the Bi-2212 to Bi-2223, as well.

- AFM investigations performed for the Bi-6 sample (obtaining the best superconducting properties) show that:
  - The thickness of the film fabricated is found to be about 900 nm.
  - The surface of the Bi-2223 superconducting film is centrally distributed and comprised of disproportionate number of peaks.

o The surface roughness of the sample is observed to be highly rough with average roughness 89.7 nm and rms roughness 96.3 nm.

Based on the results, an irregular structure is observed on the surface of the film. This irregular structure, being responsible for the change of the critical temperature and activation energy under the applied magnetic field, represents the strong anisotropic behaviour of the sample studied clearly.

- Magnetoresistivity measurements illustrate that the critical temperatures (both onset and offset) decrease with the increment of both the applied magnetic field and the angle (between the surface and applied field). The T_c^{offset} of the film without magnetic field is found to be about 102.1 K, however, it is found to decrease to 69 K (60 K) in the case of applied field perpendicular (parallel) to c-axis at the applied magnetic field of 3 T.

- The variation of $\Delta T_c (T_c^{onset} - T_c^{offset})$ increase with ascending the applied magnetic field and the effect is more prominent for the field parallel to the c-axis of the film studied, indicating that flux flow phenomenon is more dominant in $\mu_0 H // c$-axis (90°) compared to $\mu_0 H \perp c$-axis (0°).

- Both the $\mu_0 H_{irr}(0)$ and $\mu_0 H_{c2}(0)$ values obtained are noticed to decrease with the enhancement of the angle up to 90°. The former is found to reduce from 12.37 T to 6.98 T; likewise, the latter is obtained to degrade from 332.97 T to 51.94 T as a result of the anisotropic nature of the Bi-2223 superconducting film.

- The coherence lengths (ξ_0) theoretically calculated monotonously increase from 9.94 Å to 25.17 Å while the penetration depths λ_0 systematically enhance from 51.57 Å to 68.69 Å with the increment in the amount of the

83

angle, pointing out the anisotropic behaviour of the Bi-2223 thin film prepared in this work.

- The activation energy calculated from the TAFC model is observed to be about 2405 K at zero magnetic field (μ_0H=0). However, this value decreases to 439 K and 64 K in the case of applied field perpendicular (parallel) to c-axis at 3 T magnetic field applied. The field and angle dependence of the activation energy may be consistent with the intergrain weak links, grain misorientations and the strong anisotropic behaviour of the film studied.

- According to the power law, the field dependence of the activation energy for the Bi-2223 superconducting thin film produced in this work is described as nearly 0.5, meaning that the activation energy can be related to the plastic deformation of flux line lattice at dislocations, similar to the thermally activated motion of edge dislocations in crystals.

- The J_c of the film is obtained to be 2068 A/cm^2 without applied field at 4.2 K; however, it suddenly decreases to 1982 A/cm^2 (1120 A/cm^2) at the applied field value of 10mT in the case of applied field parallel (perpendicular) to c-axis, presenting that the anisotropic J_c behavior of the film is intrinsic. Further, the J_c values for all the angles changed are found to reduce sharply up to 0.4 T beyond which the change of the J_c values remains nearly constant due to the penetration of the applied magnetic field into the intergranular media below 0.4 T only.

- Flux pinning force analyze performed by Kramer equation displays that the pinning force of the superconducting film enhances with the increase of both the applied magnetic field and angle between the film surface and the field. The greatest pinning force of 17.5 MN/m^3 is observed in the case of applied

field parallel to c-axis (μ_0H//c-axis) at the applied magnetic field of 7 T due to the anisotropic nature of the film studied.

REFERENCES

[1] H. K. Onnes, Commun. Phys. Lab. Univ. Leiden **12**, 120 (1911).

[2] A.K. Saxena, *High-Temperature Superconductors*, (Springer-Verlag, 2012).

[3] W. Meissner, R. Ochsenfeld, Nature 132, 931 (1933)

[4] M.A. Omar, *Elementary Solid State Physics*, (Addison-Wesley, 1993).

[5] M. Erdem, Ph. D. Thesis (Abant Izzet Baysal University, Bolu, 2009).

[6] P. J. Ford, G. A. Saunders, Contemp. Phys. **38,** 63 (1997).

[7] F. London H. London, Proc. Roy. Soc. **A149,** 71 (1935).

[8] J. Bardeen, L. N. Cooper, J. R. Schrieffer, Phys. Rev. **108,** 1175 (1957)

[9] V. L. Ginsburg, L. D. Landau, Zh. Eksp. Teor. Fiz. **20,** 1064 (1950).

[10] R. A. Serway, *Physics for Scientists and Engineers*, 6th edn. (Brooks Cole, 2003).

[11] P. G. deGennes, *Superconductivity of Metals and Alloys*, (Westview Press, 1999).

[12] C. Kittel, *Introduction to Solid-State Physics*, 8th edn. (Wiley, New York 2004).

[13] T. P. Sheahen, *Introduction to High-Temperature Superconductivity*, 1st edn. (Springer, 1994)

[14] H. Thomas, *Earlier and Recent Aspects of Superconductivity*, (Springer-Verlag, 1990).

[15] J.G. Bednorz, K.A. Muller, Z. Phys. **64,** 189 (1986).

[16] M.K. Wu, J.R. Ashburn, C. Torng, Phys. Rev. Lett. **58,** 908 (1987).

[17] C. Michel, Z. Phys. B, Condensed Matter **68**, 421 (1987).

[18] H. Maeda, Y. Taraka, Jpn. Appl. Phys., **27**, L209 (1988).

[19] K. Tokano, Appl. Phys. Lett., **53,** 1329 (1988).

[20] J.G. Bednorz, K.A. Muller, Rev. Mod. Phys. **60,** 585 (1988).

[21] D. Yegen, A. Varilci, M. Yılmazlar, C. Terzioglu, I. Belenli, Physica C **466,** 5 (2007).

[22] I. Karaca, S. Celebi, A. Varilci, A.I. Malik, Supercond. Sci. Technol. **16,** 100 (2003).

[23] A. Varilci, M. Altunbas, O. Gorur, I. Karaca, S. Celebi, Phys. Status Solidi A **194,** 206 (2002).

[24] V. Mihalache, G. Aldica, J. Optoelectron. Adv. Mater. **9,** 919 (2007).

[25] M. Okada, Sci. Technol. **13,** 29 (2000).

[26] B. Chanda, T.K. Dey, Magn. Supercond. Mater. **A-B,** 295 (2000).

[27] A. Sedky, Physica C **468,** 1041 (2008).

[28] S.E. Mousavi Ghahfarokhi, M. Zargar Shoushtari, Physica B **405,** 4643 (2010).

[29] J.B. Torrance, Y. Tokura, S. Laplaca, T.C Huang, R.J. Savoy, A.I. Nazzal, Solid State Commun. **66**, 703 (1988).

[30] A. Kilic, Ms. Thesis (AnkaraUniversity, Ankara, 2000).

[31] S. Koyama, U. Endo, T. Kawai1, Jpn. J. Appl. Phys. **27,** L1861 (1988).

[32] M. Yilmazlar, H.A. Cetinkara, M. Nursoy, O. Ozturk, C. Terzioglu, Physica C **442,** 101 (2006).

[33] V.P.S. Awana, S.K. Agarwal, R. Ray, S. Gupta, A.V. Narlikar, Physica C **43,** 191 (1992).

[34] S. Vinu, P.M. Sarun, R. Shabna, P.M. Aswathy, J.B. Anooja, U. Syamaprasad, Physica B **405,** 4355 (2010).

[35] K.A. Sarkar, I. Maartense, T.L. Peterson, B. Kumar, J. Appl. Phys. **66,** 3717 (1989).

[36] C.K. Rhee, C.J. Kim, H.G. Lee, I.H. Kuk, J.M. Lee, I.S. Chang, C.S. Rim, P.S. Han, S.I. Pyun, D.Y. Won, Jpn. J. Appl. Phys. **28,** L1137 (1989).

[37] E. Giannini, E. Bellingeri, R. Passerini, R. Flükiger, Physica C **315,** 185 (1999).

[38] I.V. Kityk, J. Phys. Condens. Mat. **6,** 4119 (1994)

[39] M.A. Aksan, M.E. Yakinci, A. Guldeste, Thin Solid Films **515,** 8022 (2007).

[40] H. El Alami, I. Rannou, C.D. Cavellin, Physica C **406,** 131 (2004).

[41] A.M. Saleh, M.M. Abu-Samreh, M.H. Soliman, A.A. Leghrouz, R.M.L. Ketaneh, S. Darwish, M.I. Abu Taha, Thin Solid Films **468,** 93 (2004).

[42] Y. Hakuraku, Y. Shimada, M. Itoh, Supercond. Sci. Technol. **10,** 325 (1997).

[43] M. Sugano, K. Osamura, W. Prusseit, R. Semerad, K. Itoh, T. Kiyoshi, Supercond. Sci. Technol. **18,** 369 (2005).

[44] M.E. Yakinci, Y. Balci, M.A. Aksan, Y. Aydogdu, H. Ates, J. Low, Temp. Phys. **117,** 645 (1999).

[45] Y. Iijima, K. Kakimoto, Y. Sutoh, S. Ajimura, T. Saito, Supercond. Sci. Technol. **17,** S264 (2004).

[46] A. Kursumovic, R.I. Tomov, R. Huhne, J.L. MacManus-Driscoll, B.A. Glowacki, J.E. Evetts, Supercond. Sci. Technol. **17,** 1215 (2004).

[47] G. Leroy, J. Gest, L.K.J. Vandamme, J.C. Carru, Physica C **425,** 27 (2005).

[48] A.N. Jannah, S.A. Halim, H. Abdullah, Eur. J. Sci. Res. **29,** 438 (2009).

[49] V. Hakuraku, Z. Mori, S. Oku, Supercond. Sci. Technol. **6,** 408 (1993).

[50] S.G. Jung, S.W. Park, W.K. Seong, Mahipal Ranot, W.N. Kang, Y. Zhao, S.X Dou, Supercond. Sci. Technol. **22,** 075010 (2009).

[51] M. Runde, IEEE Trans. Appl. Supercond. **5,** 813 (1995).

[52] A. Godeke, D. Cheng, D.R. Dietderich, C.D. English, H. Felice, C.R. Hannaford, S.O. Prestemon, G. Sabbi, R.M. Scanlan, Y. Hikichi, J. Nishioka, T. Hasegawa, IEEE Trans. Appl. Supercond. **18,** 516 (2008).

[53] H. Miao, M. Meinesz, B. Czabai, J. Parrell, S. Hong, AIP Conf. Proc. **986,** 423 (2008).

[54] A. Tsukamoto, K. Imagawa, M. Hiratani, K. Kanehori, K. Takagi, Jpn. J. Appl. Phys. **30,** L830 (1991).

[55] J.M. Tarascon, Y. Lepage, L.H. Greene, B.G. Bagley, P. Barboux, D.M. Hwang, G.W. Hull, W.R. Makinnon, M. Giroud, Phys. Rev. B **38,** 2504 (1988).

[56] Zs. Oszi, S. Benacka, V. Strbık, S. Chromik, M. Spankova, I. Kostic, P. Kleja, Thin Solid Films **433,** 359 (2003).

[57] H.U. Habermeier, J. Supercond. Novel Magn. **13,** 871 (2000).

[58] H. Yamasaki, K. Endo, S. Kosaka, M. Umeda, S. Misawa, S. Yoshida, K. Kajimura, IEEE Tran. Appl. Supercond. **7,** 1536 (1993).

[59] T.D. Dzhafarov, A. Varilci, M. Sadigov, M. Altunbas, Physica C **268,** 143 (1996).

[60] A. Oota, M. Funakura, J. Iwaya, H. Matsui, K. Mitsuyama, Physica C **212,** 23 (1993).

[61] P. Schmitt, P. Kummeth, L. Schultz, G. Saemann-Ischenko, Phys. Rev. Lett. **67,** 267 (1991).

[62] W. Knoll, R. C. Advincula, *Functional Polymer Films*, 1st Edn. (Wiley-VCH, 2011)

[63] K.L. Choy, Prog. Mater. Sci. **48,** 57 (2003).

[64] M. Leskela, H. Molsa, L. Niinisto, Supercond. Sci. Technol. **6,** 627 (1993).

[65] A. Perrin, M. Guilloux-Viry, X. Castel, C. Le Paven-Thivet, Microelectron. J. **27,** 343 (360).

[66] G. Yildirim, M. Akdogan, S.P. Altintas, M. Erdem, C. Terzioglu, A. Varilci, Physica B **406,** 1853 (2011).

[67] A. Guldeste, M.J. Gorine, J. Cryst. Growth. **257,** 129 (2003).

[68] H. Martinez, A. Marino, J.E. Rodriguez, Physica C **568,** 408 (2004).

[69] M.A. Aksan, S. Altin, M.E. Yakinci, A. Guldeste, Y. Balci, Mater. Sci. Tech. Lond. **27,** 314 (2011).

[70] S.V. Vonsovsky, Y.A. Izyumov, E.Z. Kurmaev, E.H. Brandt, A.P. Zavarnitsyn, *Superconductivity of Transition Metals: Their Alloys and Compounds*, 1st Edn. (Springer, 2012)

[71] A. Guldeste, C.R.M. grovenor, M.J. Goringe, Supercond. Sci. Tech. **7,** 668 (1994)

[72] V. Hakuraku, Z. Mori, S. Oku, Supercond. Sci. Technol. **6,** 408 (1993).

[73] M. Souissi, G. Schmerber, A. Derory, B. El Jani, J. Magn. Magn. Mater. **324,** 2539 (2012).

[74] A. Sartori, N. El Habra, C. De Zorzi, S. Sitran, M. Casarin, G. Cavinato, C. Sada, R. Gerbasi, G. Rossetto, Chem. Vapor Depos. **18,** 151 (2012).

[75] C. Pflitsch, A. Nebatti, G. Brors, B. Atakan, J. Cryst. Growth **348**, 5 (2012).

[76] N. Didier, O. Thomas, J. P. Senateur, G. Delabouglise, A. Gaskov, B. Bochu, Physica C **723,** 235 (1994).

[77] Z.K. Chang, J.Q. Xiao, Y.Q. Chen, S.C. Liu, J. Gong, C. Sun, Acta Metall. Sin. **48,** 547 (2012).

[78] K. Ozawa, M. Ishizuka, N. Sakamoto, T. Ohno, T. Kiguchi, T. Matsuda, T. Konno, N. Wakiya, H. Suzuki, Funct. Mater. Lett. **5,** 1260016 (2012).

[79] M. Nagasaka, D. Iisaki, N. Sakamoto, N. Wakiya, H. Suzuki, Suzuki, Funct. Mater. Lett. **5,** 1260007 (2012).

[80] D. Min, N. Hoivik, U. Hanke, J. Electrocream. **28,** 53 (2012).

[81] C.C. Chen, G. Wang, L.R. Wang, C.H. Lu, Z.Z. Xu, J. Cream. Process. Res. **12,** 664 (2011).

[82] V. Narayanan, P. Lommens, K. De Buysser, D.E.P. Vanpoucke, R. Huehne, L. Molina, G. Van Tendeloo, P. Van der Voort, I. Van Driessche, J. Mater. Chem. **22,** 8476 (2012).

[83] D. Hanaor, G. Triani, C.C. Sorrell, Surf. Coat. Tech. **205,** 3658 (2011).

[84] E. Norbeck, Tp. Dubbs, Lg. Sobotka, Nucl. Instrum. Meth. A **262,** 546 (1987).

[85] N. Takahashi, N. Kakuda, A. Ueno, K. Yamaguchi, T. Fujii, Jpn. J. Appl. Phys. **28,** L244 (1989).

[86] Jd. Leroux, Dr. Paul, J. Membrane Sci. **74,** 233 (1992).

[87] D. Hu, Y.J. Liu, H.S. Li, X.Y. Cai, X.L. Yan, Y.D. Wang, Mater. Technol. **27,** 243 (2012).

[88] A.A. M. Farag, A. Ashery, M.A. Shenashen, Physica B **407,** 2404 (2012).

[89] S.W. Li, W. Li, G.X. Li, W.C. Li, B.L. Zhang, P.C. Chou, Physica C **478,** 60 (2012).

[90] L.B. Sheridan, J. Czerwiniski, N. Jayaraju, D.K. Gebregziabiher, K. Daniel, J. L. Stickney, D.B. Robinson, M.P. Soriaga, Electrocatalysis **3,** 96 (2012).

[91] S. Huang, Q. M. Jiang, S. Yang, C.H. Zhou, K.J. Chen, IIEE Electr. Device L. **33,** 516 (2012).

[92] J. Tupala, M. Kemell, E. Harkonen, M. Ritala, M. Leskela, Nanotechnology, **23,** 125707 (2012).

[93] K. Xu, R. Ranjith, A. Laha, H. Parala, A.P. Milanov, R.A. Fischer, E. Bugiel, J. Feydt, S. Irsen, T. Toader, C. Bock, D. Rogalla, H.J. Osten, U. Kunze, A. Devi, Chem. Mater. **24,** 651 (2012).

[94] D.A. Glocker, S.I. Shah, C.A. Morgan Institute of Physics Publishing; Lslf edition (1995).

[95] Y.B. He, L.H. Wang, L. Zhang, M.K. Li, X.Z. Shang, Y.Y. Fang, C.Q. Chen, J. Alloy. Compd. **534,** 81 (2012).

[96] D.M. Mattox, *Handbook of Physical Vapor Deposition (PVD) Processing*, 2nd Edn. (William Andrew, 2010)

[97] W.K. Han, G.H. Hwang, S.J. Hong, H.H. An, C.S. Yoon, J.H. Kim, M.J. Lee, G. Hong, K.S. Park, S.G. Kang, Appl. Surf. Sci. **256,** 2649 (2010).

[98] K. Wasa, M. Kitabatake, H. Adachi, *Thin Films Material Technology: Sputtering of Compound Materials*, 1st Edn. (Springer, 2004)

[99] K. Stella, D. Burstel, S. Franzka, O. Posth, D. Diesing, J. Phys. D Appl. Phys. **42,** 135417 (2009).

[100] J.W. Seo, H.S. Oh, K.M. Kang, S.M. Moon, J.S. Kwak, K.H. Lee, W.H. Lee, Y.H. Park, H.S. Park, J. Korean Inst. Met. Ma. **46,** 683 (2008).

[101] C. Yana, B. Roderic, Appl. Phys. Lett. **100,** 232112 (2012).

[102] L. Mechin, C. Adamo, S. Wu, B. Guillet, S. Lebargy, C. Fur, J.M. Routoure, S. Mercone, M. Belmeguenai, D.G. Schlom, Phys. Status Solidi A, **209,** 1090 (2012).

[103] H.M. Sohail, Ms. Thesis (Institute of Technology Linköpings Universitet, Linköping, 2009).

[104] M. Ohring, *Materials Science of Thin Films*, 2nd Edn. (Academic Press, 2001).

[105] H.J. Quah, K.Y. Cheong, J. Alloy. Compd. **529,** 73 (2012).

[106] C.G. Kuo, C.Y. Hsu, S.S. Wang, D.C. Wen, Appl. Surf. Sci. **258,** 6952 (2012).

[107] J. Zuo, P. Keil, G. Grundmeier, Appl. Surf. Sci. **258,** 7231 (2012).

[108] K.S. Pugazhvadivu, L. Balakrishnan, K. Tamilarasan, Mater. Lett. **77,** 48 (2012).

[109] B. Houng, H.B. Chen, Ceram. Int. **38,** 801 (2012).

[110] J.S. Moodera, R. Meservey, J.E. Tkaczyk, C.X. Hao, G.A. Gibson, P.M. Tedrow, Phys. Rev. B **37,** 619 (1988).

[111] B.F. Azzouz, A. Mchirgui, B. Yangui, C. Boulesteix, B.M. Salem, Physica C **356,** 83 (2001).

[112] R. Behrisch, *Sputtering by Particle bombardment*, 1st edn. (Springer, Berlin 1981).

[113] P.M. Sarun, S. Vinu, R. Shabna, A. Biju, U. Syamaprasad, Mater Lett. **62,** 2725 (2008).

[114] N. Ichinose, K. Saito, Physica C **190,** 177 (1992).

[115] Y.L. Chen, R. Stevens, J. Am. Ceram. Soc. **75,** 1150 (1992).

[116] Y.L. Chen, R. Stevens, J. Am. Ceram. Soc. **75,** 1142 (1992).

[117] G. Yildirim, S. Bal, A. Varilci, J. Supercond. Nov. Magn. **25,** 1665 (2012)

[118] B.D. Cullity, *Element of X-ray Diffraction*, 3rd Edn. (Addition-Wesley, Reading MA, 2001).

[119] E. Yucel, C. Terzioglu, A. Varilci, I. Belenli, J. Mater. Sci. Mater El. (2011) doi:10.1007/s10854-010-0274-9.

[120] Keithley Instruments Inc., *Handbook on Low Level Measurements*, 6th Edn. (2004).

[121] M. Dogruer, G. Yildirim, O. Ozturk, C. Terzioglu, J. Supercond. Nov. Magn. (2012) doi: 10.1007/s10948-012-1719-6

[122] L. Tsarkova, A. Knoll, G. Krausch, R. Magerle, Macromolecules **39,** 3608 (2006).

[123] W.V. Zoelen, E. Polushkin, G.T. Brinke, Macromolecules **41,** 8807 (2008).

[124] I. Zalakain, J.A. Ramos, R. Fernandez, H. Etxeberria, I. Mondragon, J. Appl. Polym. Sci. **25,** 1552 (2012).

[125] M. Gulen, G. Yildirim, S. Bal, A. Varilci, I. Belenli, M. Oz, J. Mater. Sci. Mater El. (2012) doi: 10.1007/s10854-012-0768-8.

[126] M.S. Ososfky, R.J. Soulen, S.A. Wolf, J.M. Broto, J.M. Rakoto, J.C. Ousset, G. Coffe, S. Askenazy, P. Pari, I. Bozovic, J.N. Eckstein, G.F. Virshup, Phys. Rev. Lett. **71,** 2315 (1993).

[127] H. Kitaguchi, A. Matsumoto, H. Hatakeyama, H. Kumakura, Supercond. Sci. Technol. **17,** S486 (2004).

[128] G. Yildirim, M. Akdogan, S. P. Altintas, M. Erdem, C. Terzioglu, A. Varilci, Physica B **406,** 1853 (2011).

[129] J.H. Kim, S.X. Dou, D.Q. Shi, M. Rindfleisch, M. Tomsic, Supercond. Sci. Technol. **20,** 1026 (2007).

[130] G. Yildirim, A. Varilci, M. Akdogan, C. Terzioglu, J. Mater. Sci. Mater. Electron. **23,** 928 (2012).

[131] M. Inui, P.B. Littlewood, S.N. Coppersmith, Phys. Rev. Lett. **63,** 2421 (1989).

[132] T. Ishida, H. Mazaki, Phys. Rev. B **20,** 131 (1979).

[133] N.V. Vo, H.K. Liu, S.X. Dou, Supercond. Sci. Technol. **9,** 104 (1996).

[134] A. Ianculescu, M. Gartner, B. Despax, V. Bley, Th. Leby R. Gavrila, M. Modreanu, Appl. Surf. Sci. **253**, 344 (1996).

[135] J. Economy, R. Anderson, Inorg. Chem. **5,** 989 (1966).

[136] L. Shi, Y. Gu, L. Chen, Z. Yang, J. Ma, Y. Qitan, Mater. Lett. **58,** 3301 (2004).

[137] G. Yildirim, S. Bal, E. Yucel, M. Dogruer, M. Akdogan, A. Varilci, C. Terzioglu, J. Supercond. Nov. Magn. **25,** 381 (2012).

[138] G. Yildirim, E. Yucel, S. Bal, M. Dogruer, A. Varilci, M. Akdogan, C. Terzioglu, Y. Zalaoglu, J. Supercond. Nov. Magn. **25,** 231 (2012).

[139] J. Jiang, Mater. Lett. **61,** 3239 (2007).

[140] G. Yildirim, S. Bal, A. Varilci, J. Supercond. Nov. Magn. **25,** 1655 (2012).

[141] T. Kucukomeroglu, E. Bacaksiz, C. Terzioglu, A. Varilci, Thin Solid Films **516,** 2913 (2008).

[142] M.R. Persland, J.L. Tallon, R.G. Buckley, R.S. Liu, N.E. Floer, Physica C **176,** 95 (1991).

[143] M. Akdogan, C. Terzioglu, A. Varilci, I. Belenli, Physica B **405,** 4010 (2010).

[144] O. Ozturk, D. Yegen, M. Yilmazlar, A. Varilci, C. Terzioglu, Physica C **451,** 113 (2007).

[145] M. Erdem, O. Ozturk, E. Yucel, S. P. Altintas, A. Varilci, C. Terzioglu, I. Belenli, Physica B **406,** 705 (2011).

[146] C. Terzioglu, M. Yilmazlar, O. Ozturk, E. Yanmaz, Physica C **423,** 119 (2005).

[147] P. M. Sarun, S. Vinu, R. Shabna, A. Biju, U. Syamaprasad, Mater. Res. Bull. **44,** 1017 (2009).

[148] M.A. Aksan, M.E. Yakinci, K. Kadowaki, J. Supercond. Nov. Magn. **23,** 371 (2010).

[149] O. Bilgili, Y. Selamet, K. Kocabas, J. Supercond. Nov. Magn. **21,** 439 (2008).

[150] M.T. Malachevsky, C.A. Dovidio, Supercond. Sci. Technol. **18,** 289 (2005).

[151] H.J. Lim, J.G. Byrne, Physica B **229,** 294 (1997).

[152] A. Tampieri, G. Celotti, S. Lesca, G. Bezzi, T.M.G. La Torretta, G. Magnani, J. Eur. Ceram. Soc. **20,** 119 (2000).

[153] A. Biju, R.P. Aloysius, U. Syamaprasad, Supercond. Sci. Technol. **18,** 1454 (2005).

[154] M. Tachiki, S. Takahashi, Solid State Commun. **70,** 291 (1989).

[155] M.Tachiki, S.Takahashi, Solid State Commun. **72,** 1083 (1989).

[156] S. Bal, M. Dogruer, G. Yildirim, A. Varilci, C. Terzioglu, Y. Zalaoglu, J. Supercond. Nov. Magn. **25,** (2012) 847.

[157] Y. Zalaoglu, G. Yildirim, C. Terzioglu, J. Mater. Sci. Mater. Electron. (2012) doi 10.1007/s10854-012-0723-8

[158] M. Tinkham, *Introduction to Superconductivity*, 2nd Edn. (McGraw-Hill, New York, 1996).

[159] J.B. Ketterson, S.N. Song, Superconductivity, 1st edn., (Cambridge University Pres, Cambridge, 1999).

[160] R.J. Soulen Jr., S.A. Wolf, Physica C **95, 1** (1990).

[161] M. Dogruer, G. Yildirim, C. Terzioglu, J. Mater. Sci: Mater. Electron. (2012) doi: 10.1007/s10854-012-0763-0

[162] G.B. Smith, J.M. Bell, S.W. Filipczuk, C. Andrikidis, Physica C **160,** 333 (1989).

[163] S. Vinu, P.M. Sarun, R. Shabna, U. Syamaprasad, J. Alloys. Compd. **487,** 1 (2009)

[164] I. Kusevic, E. Babic, Z. Marohnic, J. Ivkov, S.X. Dou, Physica C **3035,** 235 (1993).

[165] G. Yildirim, M. Dogruer, O. Ozturk, A. Varilci, C. Terzioglu, Y. Zalaoglu, J. Supercond. Nov. Magn. **25,** 893 (2012).

[166] M. Dogruer, Y. Zalaoglu, A. Varilci, C. Terzioglu, G. Yildirim, O. Ozturk, J. Supercond. Nov. Magn. **25,** 961 (2012).

[167] M.A. Aksan, M.E. Yakinci, A. Guldeste, J. Alloy. Compd. **424,** 33 (2006).

[168] A.I. Abou Aly, M.F. Mostafa, I.H. Ibrahim, R. Awad, M.A. Al Hajji, Supercond. Sci. Technol. **15,** 938 (2002).

[169] A.J. Batista–Laeyva, R. Cobas, M.T.D. Orlando, E. Altshuler, Supercond. Sci. Technol. **16,** 857 (2003).

[170] C. Attanasio, M. Salvato, R. Ciancio, M. Gombos, S. Pace, S. Uthayakumar, A. Vecchione, Physica C **411,** 126 (2004).

[171] E.G. Alcaide, M. H. Wolpez, A.J. Batista Leyva, R.F. Jardim, P. Mune, Physica C **423,** 51 (2005).

[172] A.K. Nawazish, P. Kameli, A.A. Khurram, Supercond. Sci. Technol. **19,** 410 (2006).

[173] M.H. Pu, Y. Feng, P.X. Zhang, J.X. Wang, J.J. Du, L. Zhou, Physica C **412,** 467 (2004).

[174] V. Geshkenbein, A. Larkin, M. Feigelman, V. Vinokur, Physica C **239**, 162 (1989).

[175] M.A. Aksan, A. Guldeste, Y. Balci, M.E. Yakinci, Solid State Commun. 137, 320 (2006).

[176] R. Noetzel, K. Westerholt, Phys. Rev. B **58,** 15108 (1998).

[177] A.K. Paradhan, M. Muralidhar, Y. Feng, M. Murakami, K. Nakao, N. Koshizuka, Phys. Rev. B **64,** 172505 (2001).

[178] J.T. Kucera, T.P. Orlando, G. Virshup, J.N. Eckstein, Phys. Rev. B **46,** 11004 (1992).

[179] H. Yamasaki, K. Endo, S. Kosaka, M. Umeda, S. Yoshida, K. Kajimura, Phys. Rev. Lett. **70,** 3331 (1993).

[180] E. Govea-Alcaide, I. Garcia-Fornaris, P. Mune1, R.F. Jardim, Eur. Phys. J. B **58,** 373 (2007).

[181] K.C. Woo, K.E. Gray, R.T. Kampwirth, J.H. Kang, S.J. Stein, R. East, D.M. Mckay, Phys. Rev. Lett. **63,** 1877 (1989).

[182] B. Ozkurt, B. Ozcelik, J. Low Temp. Phys. **156,** 22 (2009).

[183] H. Yamasaki, K. Endo, S. Kosaka, M. Umeda, S. Misawa, S. Yoshida, K. Kajimura, IEEE Tran. Appl. Supercond. **7,** 1536 (1993).

[184] K. Takahashi, M. Konishi, A. Ibi, H. Iwai, T. Muroga, S. Miyata, T. Watanabe, Y. Yamada, Y. Shiohara, Physica C **1001**, 426 (2005).

[185] Y. Ichino, R. Honda, M. Miura, M. Itoh, Y. Yoshida, Y. Takai, K. Matsumoto, M. Mukaida, A. Ichinose, S. Horii, IEEE Tran. Appl. Supercond. **15,** 3730 (2005).

[186] Z.X. Shi, Y.X. Zhang, H. Lv, M. Xu, E.M. Choi, Sung-Ik Lee, Physica C **467,** 101 (2007).

[187] E. Martinez, P. Mikheenko, M. Martinez-Lopez, A. Millan, A. Bevan, J.S. Abell, Phys. Rev. B **75,** 134515 (2007).

[188] Y. Matsumoto, I. Shigeta, T. Abiru, Y. Terasaki, T. Akune, N. Sakamoto Physica C **163**, 388 (2003).

[189] H. Kuishima, N. Nanato, S.B. Kim, S. Murase, Y. Yamada, A. Nitta, K. Tachikawa, G. Nishijima, K. Watanabe Physica C **469,** 1515 (2009).

[190] G. Yildirim, S. Bal, M. Gulen, A. Varilci, E. Budak, M. Akdogan, Cryst. Res. Technol. **47,** 195 (2012).

[191] G. Yildirim, M. Akdogan, A. Varilci, C. Terzioglu, Cryst. Res. Technol. **45,** 1161 (2010).

[192] I. V. Tudose, P. Horvath, M. Suchea, S. Christoulakis, T. Kitsopoulos, G. Kiriakidis, J. Appl. Phys. **89,** 57 (2007).

[193] M. Gokcen, S. Bal, G. Yildirim, M. Gulen, A. Varilci, J. Mater. Sci: Mater. Electron. (2012) doi: 10.1007/s10854-012-0690-0

[194] C.S. Yadav, P.L. Paulose, New J. Phys. **11,** 103046 (2009).

CIRRICULUM VITAE

Gürcan YILDIRIM

Address:

Abant İzzet Baysal University

Department of Physics,

Golkoy-Bolu, TURKEY

Phone: +90 374 2541000 – 2737

Fax: +90 374 2534642

e-mail: yildirim_g@ibu.edu.tr

Personal Details:

Gender: Male
Date of birth: 4th of April, 1982
Place of birth: Isparta, Turkey

Education:

2003-2007 Undergraduate Studies in Physics at Middle East Technical University

2007-2009 MSc in Physics at Süleyman Demirel University

Thesis: Investigation of the reaction cross-sections and the neutron emission spectra

of the neutrons produced in proton induced reactions of some amphoter

group target nuclei

2009-2012 PhD in Physics at Abant İzzet Baysal University

Dissertation: Electrical and magnetic properties of Bi(Pb)SrCaCuO superconductor

thin film produced by sputtering method

Specialization: Type II Superconducting materials.

Selected Publications:

1. **G. Yildirim**, A. Varilci, M. Akdogan, C. Terzioglu "Role of annealing time and temperature on structural and superconducting properties of (Bi, Pb)-2223 thin films produced by sputtering", J. Mater. Sci: Mater. Electron. (2012) 23: 928–935.

2. **G. Yildirim**, M. Akdogan, S.P. Altintas, M. Erdem, C. Terzioglu, A.Varilci "Investigation of the magnetic field angle dependence of resistance, irreversibility field, upper critical field and critical current density in DC sputtered Bi-2223 thin film", Physica B (2011) 406: 1853–1857.

3. **G. Yildirim**, S. Bal, A. Varilci, "Effect of Annealing Time and Temperature on Microstructural and Superconducting Properties of (Bi,Pb)-2212 Thin Films Produced by Magnetron Reactive Sputtering", J. Supercond. Nov. Magn. (2012) 25: 1655–1663.

4. **G. Yildirim**, S. Bal, A. Varilci, "Effect of Magnetic Field Direction on Magnetoresistivity, Activation Energy, Irreversibility and Upper Critical Field of Bi-2212 Thin Film Fabricated by DC Sputtering Method", J. Supercond. Nov. Magn. (2012) 25: 1665–1671.

5. **G. Yildirim**, M. Akdogan, A. Varilci, C. Terzioglu, "Investigation of the magnetic field angle dependence of resistance and activation energy of DC-sputtered Bi-2223 thin film", (Accepted Paper, 2012), Arab. J. Sci. Eng.

Selected Presentations:

1. M. Erdem, M. Akdogan , **G. Yildirim**, S.P. Altintas, A. Varilci , C. Terzioglu, "Investigation of the magnetic field angle dependence of resistance, irreversibility field, upper critical field and critical current density in DC sputtered Bi-2223 thin film, Bulletin of the American Physical Society, (2012).

2. **G. Yildirim**, S. Bal, Y. Zalaoglu, M. Akdogan, C. Terzioglu, A. Varilci, "Revealing three-dimension (3D) and anisotropic behavior of DC Sputtered Bi-2223 Thin Film", 5. Ulusal Süperiletkenler Sempozyumu, İzmir Yüksek Teknoloji Enstitüsü, İzmir (2011).

3. M. Akdogan, **G. Yildirim**, O. Ozturk, M. Erdem, A. Varilci, C. Terzioglu, and I. Belenli, "The effect of annealing temperature and annealing time on thin film Bi-2223 samples preparation", 4. Ulusal Süperiletkenler Sempozyumu, Karadeniz Teknik Üniversitesi, Trabzon (2009).